Depositional and geomorphic patterns of mixed calciclastic-siliciclastic systems on a deep-water Equatorial Margin

Roberto Loza Espejel[a,*], Tiago M. Alves[a] and Marco Antonio Caçador Martins-Ferreira[b]

[a] 3D Seismic Lab, School of Earth and Environmental Sciences, Cardiff University, Main Building – Park Place, CF10 3AT, Cardiff, United Kingdom

[b] Faculdade de Ciências e Tecnologia, Universidade Federal de Goiás, Conde dos Arcos, 74968755, Aparecida de Goiânia, GO, Brazil

*Corresponding author:

Mobile phone: +44 7479 746160.

E-mail address: lozaespejelr@cardiff.ac.uk and lozaespejelr@gmail.com

Keywords: *Equatorial Brazil; carbonate shelf; channel-levee systems; calciclastic depositional systems; deep-water basins*

ABSTRACT

Distal slope and basin depositional systems in deep waters of the Pará-Maranhão Basin, Equatorial Brazil, are investigated using a high-resolution 3D seismic volume, borehole data and multispectral satellite imagery. A Neogene calciclastic submarine fan and a series of channel-levee systems are analysed at water depths of 100 m to 3,500 m. Channel-levee systems have sinuous and straight morphologies and are of different sizes. Their origin is related to turbidity flows sourced and funnelled from the carbonate shelf to submarine canyons and gullies, as well as from areas with marked slope instability. A mixed calciclastic-siliciclastic sediment input is recognised with autochthonous calcarenites and calcilutites comprising the bulk of sediment on the mid and outer continental shelf. Minor amounts of siliciclastic sediment sourced from small rivers occur on the inner shelf. Sedimentation processes of a distally steepened carbonate ramp are discussed considering a general depositional setting dominated by fluctuations in relative sea level. Cross-sectional and planar

parameters of mixed calciclastic-siliciclastic channel-levee systems are compared to their siliciclastic counterparts. Morphological results show similarities between calciclastic and siliciclastic channel-levee systems. As a corollary, three types of channel-levee systems are described: (1) channels related to calciclastic submarine fans, (2) low-sinuosity, aggradational channels, and (3) high-sinuosity channels.

1 Introduction

Deep-water channel-levee systems develop beyond continental shelves (Lemay et al., 2020), where sediment is transported from shallow waters into deep and ultra-deep water basins; described by Pettingill (2006) as ranging in depth from 500 m to 2,000 m, and extending beyond 2,000 m, respectively. Research on siliciclastic depositional systems has been generally the centre of attention in deep-water basins, with studies on calciclastic systems lagging behind the latter (Payros and Pujalte, 2008). Furthermore, when compared to carbonate-platform settings, deep-water carbonate systems are also less documented and poorly understood (Playton et al., 2010). Yet, deep-water calciclastic systems have recently regained interest in industry and academia due to the need of integrating deep-water deposits in global and local models of carbonate depositional systems. Such models are crucial as new hydrocarbon exploration plays are being sought beyond the more-common shallow carbonate depositional settings (Reijmer et al., 2015a).

Deep-water carbonate systems are key to understand the growth, evolution and depositional conditions of carbonate systems as a whole, and can be used to document the relationship between basin and platform settings (Playton et al., 2010). In fact, calcium carbonate ($CaCO_3$) is a significant source of sediment to the present-day ocean with an estimated discharge of about 5 billion tons (bt) per year, of which 3bt accumulate in sediments,

and the other 40% is dissolved (Milliman, 1993; Jorry et al., 2020). Deep-water carbonate depositional systems (i.e. carbonate slopes and basins) can be categorised and subdivided based on their type of deposit, large-scale stratal patterns, and spatial architecture. Playton et al. (2010) grouped deep-water carbonate systems taking into account their dominant type of deposit: debris, grain- and mud-dominated. Spatial architecture in these settings are documented by Playton at al. (2010) and range from strike-continuous aprons to discontinuous tongues and channel-fan complexes. Calciclastic submarine fans and channel-levee systems are particularly less documented than slope aprons; they have been largely overlooked as they were, thus far, thought to be rare in the stratigraphic record (Payros et al., 2007; Payros and Pujalte, 2008; Back and Reuning, 2015; Dunlap et al., 2018).

Published work aiming to understand deep-water carbonate depositional systems include vintage articles with initial descriptions of carbonate slopes (e.g. Ditty et al., 1977; James and Mountjoy, 1983; Ravenne et al., 1985; Kenter, 1990; Coniglio and Dix, 1992), important compilations (Payros and Pujalte, 2008; Playton et al., 2010; Reijmer et al., 2015a) and recent studies in which depositional models separate carbonate settings from their siliciclastic counterparts (Mulder et al., 2014; Counts et al., 2019; Moscardelli et al., 2019; Jorry et al., 2020). For instance, the modern and ancient Bahamian sedimentary system has been crucial to understand carbonate platform-to-basin sedimentation patterns, and recognise that carbonate-lobe and channel systems are able to develop in deep-water basins (Bornhold and Pilkey, 1971; Crevello and Schlager, 1980; Eberli et al., 1997, 2005; Betzler et al., 1999, 2014; Mulder et al., 2012, 2014; Reijmer et al., 2015a; Wunsch et al., 2017). Ancient outcrop examples have also been used to document calciclastic systems such as the Miocene Azagador Formation in southern Spain (Braga et al., 2001), the Eocene Anotz Formation in the western Pyrenees (Payros et al., 2007), and the Miocene Albacore slope fan in SE Australia (Gallagher et al., 2001).

New investigations based on high-quality seismic data have increased our knowledge of deep-water carbonates in areas such as the Browse Basin, Northwest Shelf of Australia, with carbonate deep-water channel-levee systems having been reported in Miocene strata (Back and Reuning, 2015; Rankey, 2017; Dunlap et al., 2018; Janson et al., 2018; Rinke-Hardekopf et al., 2018; Tesch et al., 2018; Zeng, 2020). In addition, Mulder et al (2014) and Wunsch et al. (2017) described a modern channel-levee system in the pure carbonate setting of the Bahamas Archipelago. Ultra-deep-water carbonate deposits are relatively less documented, but recent investigations have pointed out their existence in the form of channel-levee complexes and turbiditic lobes at water depths of 2,000 m to 3,400 m around isolated carbonate platforms in the Indian Ocean (Counts et al., 2019; Jorry et al., 2020). Despite these efforts, geomorphological and architectural features of mixed carbonate-siliciclastic systems remain underexplored in the literature, possibly due to incomplete datasets leading to simplistic descriptions (Moscardelli et al., 2019). Mixed calciclastic-siliciclastic systems derive from the interaction between a siliciclastic source (usually river discharge) and a regional carbonate factory (Chiarella et al., 2017). These systems have been studied since the 1970s in regions such as the Hispaniola-Caicos Basin, where siliciclastic and carbonate deposits mix in the form of turbidity currents generating a deep-water fan system. In parallel, Francis et al. (2008) have presented an example of a mixed deep-water calciclastic-siliciclastic system in the Gulf of Papua, northeast Australia and southern Papua New Guinea. Here, mixed sediment derived from two different sources, resulted in the generation of channel-levee systems. More recently, Moscardelli et al. (2019) have documented a mixed siliciclastic-carbonate turbiditic depositional system offshore Nova Scotia (Back and Reuning, 2015; Dunlap et al., 2018).

This study aims to expand the current knowledge about deep- and ultra-deep water carbonate depositional systems (i.e. mixed calciclastic-siliciclastic systems) by using a case study from the Miocene to Holocene Pará-Maranhão (PAMA) Basin in Equatorial Brazil (Figs.

1 and 2). High-quality 3D seismic data are used to characterise the internal geometry of channel-levee systems formed in a mixed calciclastic-siliciclastic depositional system. Borehole data from the shelf margin document the thickness and composition variability of the so-called Ilha de Santana Platform and the PAMA continental shelf, which provide the main source of sediment to the continental slope and rise (Figs. 1 and 2). Hence, this work investigates the morphological expression of mixed calciclastic and siliciclastic sediment transfer from the PAMA shelf and the Ilha de Santana Platform, via the continental slope, on its way to deep and ultra-deep waters. Details about the Neogene stratigraphic succession of the PAMA Basin aim to provide a better understanding of new exploration plays in Equatorial Brazil. In summary, this paper intends to answer the following questions:

1. What types of depositional features characterise mixed calciclastic-siliciclastic systems in deep and ultra-deep-water environments?
2. Can deep-water channel-levee systems be formed on a carbonate-dominated continental margin recording minor siliciclastic input?
3. How similar are the geomorphic properties of channel-levee systems formed on carbonate-rich margins when compared to their siliciclastic counterparts?

As described in Playton et al. (2010), it is useful and important to understand the relationship between platform and basinal settings. This is because in many cases, platform-derived information is more robust than basin-related data. Our study area is such a case, as the continental slope and rise are imaged in seismic data, while exploration wells were, thus far, only drilled on the shelf margin (Fig. 1b).

2 Geological framework

The offshore Para-Maranhão (PAMA) Basin is located on the Brazilian Equatorial Margin and consists exclusively of marine deposits covering an area of about 48,000 km^2 (Soares et al., 2007) (Fig. 1). The basin is oriented NW-SE due to the effect of transtensional tectonics in its early development, being bounded by the Foz do Amazonas Basin to the northwest and the Barreirinhas Basin to the southeast (Zalán, 2015) (Fig. 1).

Hydrocarbon exploration started in the PAMA Basin during the 1970s and 1980s, via the acquisition of a series of 2D seismic profiles and the drilling of multiple exploratory wells. Most wells were deemed dry until the year of 1993, with the discovery of a sub-commercial oil show in fractured Cenozoic carbonates in the well 1-PAS-11 (Soares et al., 2007; Zalán, 2015). Interest in the region has increased in the past decade due to the economic potential of deep and ultra-deep water basins of Equatorial Brazil, which was enhanced by the discovery of large oil fields on the conjugate margins of Ghana and Ivory Coast (Henry et al., 2011). In fact, deep-water basins in West Africa and Equatorial Brazil have similar structural and sedimentary features (Henry et al., 2011; Zalán, 2015; Almeida et al., 2018, 2020; Da Silva and Ribeiro, 2018). In parallel, recent data in Zalán (2015) and Da Silva and Ribeiro (2018) describe a broad gravitational system in the PAMA and Barreirinhas basins, relating this same system to the deposition of overlying turbidites (e.g. GB1-4500, Figs. 1a, b and 3a).

2.1 Tectono-stratigraphic setting

The sedimentary history of the PAMA Basin is complex and started with the deposition of Paleozoic deposits over Precambrian intracratonic sequences (Soares et al., 2007; Zalán, 2015). This basin has been controlled since the Cretaceous by two major oceanic fracture zones, the Romanche and St. Paul; which are still active today (Nemčok et al., 2013). An

149 updated and detailed tectono-stratigraphic chart was published by Soares et al. (2007) in which
150 the PAMA Basin is sub-divided into three supersequences: Pre-Rift (intracratonic), Rift, and
151 Drift (Fig. 3a). Basal Paleozoic deposits from the intracratonic Pre-Rift Supersequence are
152 inferred as similar to those in the Parnaíba Basin (Zalán, 2015). The latter basin comprises
153 Paleozoic strata deposited over the São Luís Craton due to the fragmentation and breakup of
154 northwestern Gondwana (Soares et al., 2007; Oliveira et al., 2012).

155 The Rift Supersequence was deposited under a transtensional tectonic regime and is
156 divided into Aptian and Albian syn-rift (Rift II) and intra-rift (Rift III) deposits (Soares et al.,
157 2007). Syn-rift strata are composed of continental sandstones and shales showing strata pinch-
158 outs in seismic sections. In between the two rift phases (Rift II and Rift III), a sag basin was
159 developed and was filled by the Codó Formation, a unit of lagunar organic-rich shales,
160 anhydrites and calcilutites (Soares et al., 2007). Their seismic response is characterised by
161 parallel reflectors with good continuity. The Albian Rift III sequence is formed by siliciclastic
162 deposits typical of delta fans accummulated in a marine environment (Brandão and Feijó, 1994;
163 Soares et al., 2007). Comparisons with the Ceará Basin (Almeida et al., 2018, 2020) indicate
164 this latter Rift III sequence to be a Breakup Sequence *sensu* Soares et al. (2012) and Alves and
165 Cunha (2018).

166 The Late Albian to Recent Drift Supersequence comprises the Humberto de Campos
167 Group, and is divided into three units: Areinhas (sandstones), Ilha de Santana (wide carbonate
168 shelf), and Travosas formations (slope and turbidite deposits) (Soares et al., 2007; Zalán, 2015)
169 (Fig. 3c). In addition, the study area contains gravitational systems in the Drift Supersequence
170 that impose a marked structural zonation in the basin from its proximal to distal parts (Fig. 3a,
171 b). As a result; extensional, transitional and contractional zones are identified from the shelf to
172 the abyssal parts of the PAMA Basin (Zalán, 2001; Oliveira et al., 2012; Almeida et al., 2018)
173 (Fig. 3a, b).

2.2 Regional stratigraphy

Brandão & Feijó (1994) first described the stratigraphic succession of the PAMA Basin based on data from 29 exploration wells and 45,500 km of 2D seismic profiles, sub-dividing the region into three groups: Canárias, Caju and Humberto de Campos (Fig. 3c). The Canárias Group consists of sandstones, siltstones and shales deposited by deltaic fans in a marine environment during the Early and Mid- Albian (Brandão and Feijó, 1994). The Caju Group consists of quartzose sandstone, shales and local bioclastic calcarenites accumulated in a neritic environment during the late Albian (Brandão and Feijó, 1994). The Humberto de Campos Group comprises Cenomanian to Recent deposits representative of a divergent margin, and includes the Areinhas, Ilha de Santana and Travosas formations (Figs. 3c and 4). The Humberto de Campos Group extends to the Barreirinhas Basin and its youngest strata are the focus of this work.

The Areinhas Formation is composed of quartzose sandstone packages intercalated with shales, siltstone and calcilutite. The Ilha de Santana Formation comprises a thick carbonate succession with the presence of calcarenites and calcilutites intercalated with shales and marls. Turbidites are common on the continental slope. The Travosas Formation is a typical coastal-platform-slope system and, at its most distal part, is known to comprise deposits of shales and siltstones intercalated with quartzose sandstones (Brandão and Feijó, 1994; De Souza, 2006; Piovesan, 2008). However, based on the well data later described in Section 5, parts of the Travosas Formation are also dominated by calciclastic deposits. In essence, a mixed calciclastic-siliciclastic system sourced by the Ilha de Santana Platform fed the continental slope and rise as a result of slope instability, turbidity and marine currents.

2.3 Carbonate-platform development off PAMA

In the latest Cretaceous-earliest Paleogene, the main sediment input to the PAMA Basin was siliciclastic, and the Ilha de Santana Platform was still an emerged area (Soares Júnior et al., 2011). According to Soares et al. (2007), a sea-level lowstand dominated the evolution of the PAMA Basin during the upper Eocene and lower Oligocene, narrowing the carbonate shelf and exposing it to subaerial conditions. This facilitated the development of dolomitic intervals in the Ilha de Santana Formation (Soares et al., 2007).

During the late Oligocene-middle Miocene, the Equatorial Margin of Brazil was dominated by the development of a large carbonate platform in a shallow-water palaeoenvironment (Soares et al., 2007; Soares Júnior et al., 2011; Rossetti et al., 2013; Aguilera et al., 2020). This carbonate platform extended from the Foz do Amazonas Basin (Figueiredo et al., 2007; Aguilera et al., 2020), to the PAMA (Soares et al., 2007), Barreirinhas (Trosdtorf Junior et al., 2007) and the Ceará basins (Soares Júnior et al., 2011). In the Foz do Amazonas Basin, carbonate productivity terminated around the late Miocene-Pliocene as a consequence of Andean tectonics, which led to a rearrangement of the palaeo-Amazon River and the subsequent onset of clastic sediment input from both the Amazon delta and coastal plain drainage systems (Figueiredo et al., 2007; Soares Júnior et al., 2011; Aguilera et al., 2020). In the three other basins mentioned above, carbonate productivity continued until the present-day, as recorded in well data crossing the Ilha de Santana Formation (Fig. 5) and published stratigraphic data from the Ceará and Barreirinhas basins (Soares Júnior et al., 2011; Aguilera et al., 2020). In the PAMA Basin, Aguilera et al. (2020) identified minor siliciclastic input near the shore during the Miocene, sourced from small river mouths such as the Gurupí River (Fig. 1b).

3 Datasets and methods

3.1 Seismic data

This study uses a full-stack depth-converted 3D seismic volume (3D PAMA PSDM Full Stack) covering an area of about 1,950 km^2 in the PAMA Basin, Equatorial Brazil (Figs. 1a, b and 2). Our dataset images the edge of the continental shelf, together with the continental slope and continental rise, in water depths ranging from 100 m to 3,500 m (Figs. 2 and 3b). The seismic volume, provided by Polarcus, consists of 3201 inlines (IL) and 3901 crosslines (XL) with a 12.5 x 12.5 m line spacing and a sampling interval of 5 m. The interpreted seismic data were processed in the depth domain with a SEG positive polarity using the European convention; an increase in impedance is represented by a red (positive) peak (Fig. 3b). The high-quality seismic data allow for the detailed analysis of stratigraphic and seismic facies to a depth of 7,500 m below the sea floor (Fig. 3b). In this study, we focus on the Miocene to Holocene stratigraphic successions of the PAMA Basin (Figs. 3b, c and 4).

In addition to 3D seismic data, we use public 2D seismic sections to complement our study. The regional 2D seismic profile GB1-4500 was reinterpreted from Henry et al. (2011) and Zalán (2015) as to provide information on the PAMA Basin at the scale of the continental margin (Figs. 1b and 3a). Regional 2D seismic profile 022-0837 (Fabianovicz, 2013), and seismic profiles 0270-3010 and 0275-8780 (Da Silva and Ribeiro, 2018), were used to correlate the seismic stratigraphy of our study area with main depositional sequences recognised on borehole and outcrop data (Fig. 1b).

3.2 Well data

Well data are scarce in the PAMA Basin, with only a few exploration wells spudded in shallow waters of the carbonate shelf margin. No wells have been drilled on the continental

slope and rise within the interpreted seismic survey. Composite data from seven (7) exploration wells were provided by the Brazilian National Agency of Petroleum, Natural Gas and Biofuels (ANP) (Fig. 5). The exploration wells are located near the edge of the continental shelf and document the shallow-water depositional systems transporting sediment into deep waters (Fig. 5). Well data include gamma-ray, deep-resistivity and lithological logs (Fig. 5).

3.3 Seismic interpretation and channel definition

Our seismic-stratigraphic interpretation is based on published literature from Fabianovicz (2013), Da Silva and Ribeiro (2018), and Alves et al. (2020). Stratigraphic data for the basin derive from the work of Brandão & Feijó (1994), Soares et al. (2007) and university theses such as De Souza (2006), Da Silva (2007) and Piovesan (2008). A summary of the methodology used to analyse the depositional systems and geomorphic parameters of channel-levee systems is shown in Fig. 6.

The offshore PAMA Basin is still an exploration frontier with limited data available in existing publications. However, a few published 2D seismic profiles intersecting our 3D survey were useful to gain a regional understanding of the basin (Fig. 1b). In this study, we reinterpreted a portion of the GB1-4500 seismic profile to provide a regional context for the PAMA Basin (Fig. 3a). This pre-stack depth migrated (PSDM) 2D seismic profile GB1-4500 from ION's Greater Brazil SPAN project has been previously interpreted by Henry et al (2011) and Zalán (2015). Published interpretations of 2D seismic profiles 0222-0837 from Fabianovicz (2013), and 0270-3010 and 0275-0780 from Da Silva et al. (2018), provided us with additional stratigraphic information (Fig. 1b). A portion of the seismic profile 0275-8780 is shown in Fig. 5c and 5d together with a projection of well 1-MAS-16.

Seismic interpretation was completed using Schlumberger's Petrel® and based on the general principles of seismic stratigraphy; hence, we interpreted reflection terminations, seismic facies and seismic units in great detail (Cross and Lessenger, 1988; Catuneanu, 2006). In total, five key seismic horizons (H_1 to H_5) were interpreted, together with the seafloor (SF), in Miocene to Recent strata (Figs. 3b, 4 and 7). Two regional unconformities (Top Oligocene and Top Cretaceous) were also interpreted and considered to be key stratigraphic markers in the study area (Figs. 3b and 4). Channel-levee systems were mapped on specific seismic horizons (Figs. 6, 7 and 8).

Seismic interpretation near the continental slope and also within channel systems is difficult due to their complex geometries and poor continuity of seismic reflections (Fig.8). To tackle this problem, seismic attributes such as instantaneous phase and cosine of phase are computed and displayed with a certain degree of transparency over the amplitude volume, so as to better identify the continuity of particular seismic reflectors (Fig. 6). A surface grid with a cell size of 25x25 m is used to generate structural maps (Figs. 6 and 7). Based on a previously calculated variance attribute volume, the variance attribute is extracted with a search window of 20 m for every depth map (H_1 to H_5, and SF) (Fig. 6). This latter seismic attribute is crucial in our analysis as it highlights discontinuities in each seismic horizon, improving the imaging of stratigraphic features and facilitating channel recognition (Fig. 7).

Both depth and extracted variance raster maps have been imported into ArcGIS to digitise and delineate discrete channel-levee systems (Fig. 6). For an enhanced visualization, depth maps are overlayed by variance maps with a 50% transparency (Fig. 7). A 3D visualisation of key maps is also useful to better recognise channel-levee systems and other sediment conduits (Fig. 7).

3.4 Geomorphic parameters

A similar methodology to Gee et al. (2007) and Lemay et al. (2020) is adopted in this work to analyse the morphometric parameters of channel-levee systems in the PAMA Basin (Fig. 6). Lemay et al (2020) introduce a quantitative geomorphic classification and methodology to analyse submarine sediment conduits based on cross-sectional and planform data. Their classification helps to differentiate between sediment conduits with and without the presence of levees. In parallel, Gee et al. (2007) examines and quantifies key geometric parameters in deep-water submarine channels to better understand the main controls on submarine channel geometry, as well as on their initiation and evolution. The latter authors focus on siliciclastic systems, and this work aims to compare and differentiate their models to the calciclastic systems of the PAMA Basin.

Cross-sectional parameters are measured every 3 to 5 km along the channel thalwegs, in perpendicular profiles to these latter. Measurements include width (W), mean depth (Lh_{mean}), maximum depth (Lh_{max}) and area; parameters used later in this work to classify the interpreted channels (Fig.8). The upper limits of asymmetric levees are precisely defined for each channel. In our measurements, the mean depth (Lh_{mean}) is the ratio of the cross-sectional area to the bankfull width of a channel (Figs. 8 and 9).

Parameters used in this work to characterise channel planform geometries include sinuosity, meander amplitude (A) and meander wavelength (λ) and are measured using a Python Jupyter Notebook provided by Lemay et al. (2020). This algorithm is based on Sylverster and Pirmez (2017) script, allowing for consistent measurements of all studied channels. The processing steps of the Lemay et al. (2020) algorithm are as follows: (1) *x* and *y* coordinates of the channel centrelines are resampled with a 50 m spacing; (2) centrelines are smoothed out for a given window length using the Savitzky-Golay filter (Savitzky and Golay, 1964). (3) The curvatures of the centreline are computed to determine inflection points in

channels; (4) the number of channel bends are defined by computing inflection and apex points; and (5) geometric parameters (sinuosity, λ and A) are computed for each channel bend. In this work, conduit bed slope is measured every 3 to 5 km based on the thalweg depth obtained from seismic profiles. A value of about twice the mean channel width is used in Step 2 above, to scale the window length to the interpreted channels.

3.5 Statistical analysis

The morphometric parameters of the PAMA calciclastic channel-levee systems are plotted on box- and cross-plots (Figs. 10 and 11). Box plots show the statistical distribution of the morphometric parameters for each channel-levee system (Fig. 10). Cross-plots show the relationships between specific morphometric parameters (i.e. mean bankfull depth, bankfull width, meander amplitude and meander wavelength) (Fig. 11). Least-square linear regressions were computed on log-transformed data for all calciclastic channel-levee systems together, as to obtain a power-law equation (Fig. 11). A regression curve with its associated 95% confidence interval is shown only when the coefficient of determination R^2 is higher than 0.1 to avoid non-correlation hypotheses (Fig. 11).

Calciclastic morphometric relationships are compared to established models (i.e. power-law equations) of siliciclastic submarine conduits from Lemay et al. (2020) and fluvial channels from Williams (1986) and Held (2011) (Fig. 11). Data from Lemay et al. (2020) are plotted to document the differences between siliciclastic submarine conduits and calciclastic channels (Fig. 11).

4 Physiography and sedimentary environment

The modern PAMA continental shelf is 150 km to 250 km wide. Water depth along the shelf-slope profile transitions from shallow waters with an average depth of 25 m on the continental shelf to 3,500 m in ultra-deep waters (Figs.1, 2 and 3). The PAMA continental shelf is a tectonically steepened carbonate ramp with no rimmed reef along its margin (Alves et al., 2020). The study area has been considered as a mixed carbonate-siliciclastic shelf in all similar to the analogous Ceará Basin (de Morais et al., 2019) (Fig.1a).

Recent data from Ceará identified three main depositional systems on its continental shelf: a) siliciclastic, located near the shoreface and river mouths, b) mixed, comprising biolithoclastic and lithobioclastic facies and, c) carbonate, revealing the predominance of an autochthonous carbonate supply, mainly derived from calcareous algae (de Morais et al., 2019). The modern carbonate shelf of Equatorial Brazil is itself considered to be a major supplier of carbonate deposits to more distal regions as its middle and outer parts record typical autochthonous carbonate sedimentation (de Morais et al., 2019). The inner continental shelf is characterised by the mixing of siliciclastic and carbonate sediment, especially during maximum freshwater discharges from suspended sediment released from river mouths (de Morais et al., 2019). An exception to this setting is the Foz do Amazonas Basin, which is dominated at present by the large siliciclastic input from the Amazon River and Delta, feeding sediment into deep waters via a large submarine channel (Fig. 1a).

Siliciclastic input from rivers such as Gurupí and Turiaçu in PAMA can be compared to the depositional setting observed in Ceará, as they have similar settings (Fig. 1c). In Ceará, the transporting distance of suspended sediment sourced from near the shoreline have been studied around the Parnaíba and Jaguaribe rivers, where siliciclastic material is transported up to 10 km oceanward from the river mouths (Dias et al., 2013; Aquino da Silva et al., 2015) (Fig. 1a). In order to verify how far siliciclastic sediment can travel on the modern PAMA shelf today,

364 we used a comparable approach to Aquino da Silva et al. (2015) and Morais et al. (2019) (Fig.
365 1c). In this work, we utilised a combination of multispectral satellite imagery with bands B4-
366 Red, B3-Green, and B1-Ultra blue (coastal aerosol) provided by the Sentinel-2 mission (Fig.
367 1c). Sediment suspended in water can be traced by using the coastal aerosol band (B1), as this
368 band reflects the blue and violet colour spectra displaying subtle differences in the colour of
369 water (Hedley et al., 2018). The interpreted multispectral satellite data prove that sediment
370 from rivers in PAMA is transported 20 km to 50 km off the shoreline (Fig. 1c). This pattern is
371 similar to that observed on the Ceará continental shelf (de Morais et al., 2019, Fig. 1),
372 suggesting that the inner shelf in PAMA is also dominated by the deposition of siliciclastic
373 sediment (Fig. 1c).

374 Well data from PAMA document the presence of calcarenite and calcilutite deposits on
375 the outer continental shelf (Fig. 5). In PAMA, there are no scuba diving or sedimentary cores
376 such as the ones analysed in Ceará by de Morais et al. (2019), but the well data shown in this
377 paper still reveals similar depositional systems to those recognised in Ceará. On both the
378 PAMA and Ceará basins, the middle and outer continental shelf reveal the predominance of
379 autochthonous carbonate sediment (de Morais et al., 2019).

380 Based on the observations above, we can suggest that beyond the inner 50 km zone of
381 the PAMA continental shelf, dominated by episodical siliciclastic input, there is a healthy
382 development of a carbonate depositional system such as the one observed off Ceará. In our
383 study area, this carbonate system extends up to 150 km to 165 km away from the inner zone,
384 and occurs on the herein called middle and outer continental shelf (Fig. 1c). Beyond the shelf
385 edge, submarine canyons develop on the continental slope and transition to channel-levee
386 systems in ultra-deep waters (Fig. 2). The outer continental shelf, dominated by carbonate
387 deposition with calcarenites and calcilutites, is the primary sediment source feeding the
388 channel-levee systems recognised beyond the shelf edge. Deep-water depositional systems in

PAMA can be considered as pure carbonate systems given the presence of a wide area of carbonate deposition on the Ilha de Santana Platform. However, because of the presence of siliciclastic deposits on the inner continental shelf, it is more conservative to consider these same deep-water depositional systems as mixed calciclastic-siliciclastic. This is because siliciclastic input can be transported away from the inner shelf to the proximity of the shelf break and upper continental slope due to marine currents acting on the shelf, such as the documented in the Gulf of Papua and North Queensland, Australia (Francis et al., 2008). Additional data such as piston core samples would be useful to confirm this interpretation.

5 Borehole stratigraphic interpretation

Seven (7) exploration wells provide important stratigraphic data in the study area and complement the stratigraphic column in Soares et al. (2007) (Figs. 4 and 5). Well 1-MAS-9 drilled 1658 m of strata in the Ilha de Santana Formation comprising thick successions of calcarenites with intercalated packages of calcilutites (Fig. 5). Below this latter unit, Well 1-MAS-9 crossed a thin package of the Travosas Formation consisting of carbonate deposits (calcarenites and calcilutites) intercalated with sandstone intervals up to 3 m-thick (Fig. 5). This is an important observation because it shows carbonate deposition to predominate on the continental slope of PAMA, a character contrasting with previous interpretations of the Travosas Formation as a siliciclastic-dominated unit (e.g. Brandão and Feijó, 1994; De Souza, 2006; Piovesan, 2008).

Well 1-MAS-16 found 3450 m of Paleogene-Neogene strata in the Ilha de Santana Formation consisting of thick packages of calcarenites intercalated with thin layers of calcilutites and calcisiltites with sparse layers of marls and dolomite (Fig.5). Towards the base of the formation there are more frequent, and thicker calcisiltite intervals. Well 1-MAS-16 is

413 the only well with available chronostratigraphic data, although only for Cretaceous strata
414 (Piovesan, 2008). Here, the Travosas Formation shows a greater presence of siliciclastic
415 material, mainly intervals of shale and marl intercalated with calcisiltite layers (Fig. 5). Well
416 1-MAS-16 is also important as it can be projected and tied to seismic profile 0275-8780 from
417 Da Silva and Ribeiro (2018) (Fig. 5c, d). Paleocene-Oligocene strata appear to be dominated
418 by the development of a thick carbonate shelf. Miocene to Recent strata reveal the aggradation
419 of a growing, healthy carbonate shelf (Fig. 5c, d).

420 Well 1-MAS-19 found 3193 m of strata in the Ilha de Santana Formation, which
421 comprises calcarenites in its upper part (Fig. 5). Below a depth of 2140 m, the Ilha de Santana
422 Formation reveals significant siliciclastic input in the form of 5 m- to 10 m- thick layers of
423 sandstones and marls (Fig. 5). Well 1-MAS-19 also drilled through 603 m of intercalated
424 sandstones, siltstones and shales in the Travosas Formation (Fig. 5).

425 Wells 1-MAS-24 and 1-MAS-10 respectively drilled 4108 m and 3946 m of the Ilha de
426 Santana Formation in the thickest part of the continental shelf (Fig. 5). In contrast, wells 1-
427 MAS-25 and 1-MAS-27A drilled the thinnest portion of the carbonate shelf, recording 1252 m
428 and 1630 m of intercalated calcarenite and calcilutite packages (Fig. 5). Thin layers of
429 sandstone and shale are observed in these two wells, suggesting episodic pulses of siliciclastic
430 material transported from the inner continental shelf to its outer part. Wells 1-MAS-25 and 1-
431 MAS-27A also reveal the presence of a 97 m and 110 m thick Areinhas Formation, chiefly
432 consisting of sandstone and shale (Fig. 5).

433 Well 1-MAS-25 found 183 m of the Travosas Formation with intercalations of sandstone,
434 shales and calcarenites (Fig. 5). The Travosas Formation in wells 1-MAS-9 and 1-MAS-25
435 documents that, during the Maastrichtian, there was a mixed carbonate-siliciclastic
436 depositional system on the upper continental slope of the PAMA Basin. In addition, the seven

437 wells interpreted in this work confirm the presence of a thick Cenozoic carbonate shelf in the
438 study area, with thin siliciclastic deposits. This suggests that distal slope deposits in the
439 Miocene to Recent PAMA Basin are mainly dominated by redeposited calciclastic sediments
440 with occasional compositional mixing with siliciclastic deposits (Fig. 5).

441

442 6 Seismic-stratigraphic framework of PAMA

443 Four Miocene-Holocene seismic units were interpreted in the PAMA Basin and named,
444 from the oldest to the youngest, as Units 1 to 4 (Figs. 3b and 4). These stratigraphic units lie
445 on top of the gravitational complex imaged in Fig. 3b. The Top Cretaceous (TK) horizon was
446 mapped first to provide a key reference to our structural analysis (Fig. 3b, c). The Top
447 Oligocene (TO) horizon marks a major regional unconformity in the PAMA Basin caused by
448 a global sea-level fall (Gradstein et al., 2005; Soares et al., 2007) (Fig. 3b). Faults related to
449 the slope gravitational complex terminate at horizon TO (Fig. 3b). In the study area, the
450 unconformity forms a high amplitude reflector with onlapping strata above it (Fig. 3b), as also
451 recognised in the Barreirinhas and Foz do Amazonas Basins (Soares et al., 2007; Da Silva and
452 Ribeiro, 2018). Above the TO unconformity, a general aggradational setting for the PAMA
453 carbonate shelf has been previously suggested by Soares et al. (2007).

454 Multiple channel-levee systems occur close to or on Miocene to Recent horizons H_1 to
455 H_5 (Fig. 7). These systems occur in Seismic Units 1 to 4 described below. Based on descriptions
456 in Soares et al. (2007) and Rosetti et al. (2013), we have correlated our seismic units to the
457 sequences defined in Soares et al. (2007) (Fig. 4).

458

6.1 Unit 1 - Lower Miocene

Unit 1 is characterised by its high to medium sub-parallel internal reflections. It is bounded at its base by the TO horizon and onlaps this latter unconformity to the southwest (Fig. 3b). Horizon H_1 marks the top of Unit 1 and comprises a high amplitude, sub-parallel seismic reflector (Fig. 7k, l).

Unit 1 is correlated with Sequence E80-N10 in Soares et al (2007), recognised as a major Cenozoic transgressive event (Fig.3). This event is associated with the maximum expansion of carbonate deposition on the PAMA continental shelf. On the continental slope, horizon H_1 is characterised by the incision of a small and sinuous channel and the formation of a calciclastic submarine fan as shown in Figs. 7k and 7l.

6.2 Unit 2 - Middle Miocene

Middle Miocene strata in Unit 2 is bounded by horizons H_1 and H_3, and onlaps the Top Oligocene unconformity to the southwest (Figs. 3b and 4). This unit has medium- to high-amplitude reflections, and is correlated with Sequence N20-N30 defined in Soares et al. (2007). Horizon H_2 is observed half-way through Unit 2 as a low- to high- amplitude discontinuous reflection. The formation of a large channel (channel *c*) is first observed at the level of horizon H_2 (Fig. 7i, j).

The top of Unit 2 coincides with horizon H_3, a moderate-amplitude reflector (Fig. 4). This unconformity has been considered as an important feature on Brazil's Equatorial Margin in seismic and well data (Soares et al., 2007). Although its amplitude is not as high as the Top Oligocene (TO) unconformity, horizon H_3 marks a relative sea-level drop across the PAMA Basin (Figs. 3b and 7g, h).

6.3 Unit 3 - Upper Miocene-Pliocene

Unit 3 correlates with Sequence N40-N50 in Soares et al. (2007) (Fig. 4). The unit is bounded at its base by horizon H_3 and at its top by horizon H_5 (Fig. 4). Strata in this unit mark a phase of progradation of the PAMA continental shelf (Soares et al., 2007). A low- to medium-amplitude, sub-parallel reflector (Horizon H_4) separates Upper Miocene and Pliocene strata within Unit 3 (Figs. 3b and 4). Horizon H_4 is incised by Holocene channels and canyons on the continental slope.

6.4 Unit 4 Pleistocene to Recent

Pleistocene to recent strata lie above horizon H_5, a medium-amplitude continuous reflector. The seafloor (SF) bounds Unit 4 at its top. This unit has low-amplitude continuous reflections and correlates with Sequence N60 in Soares et al. (2007) (Fig. 4).

7 Morphology of calciclastic submarine fans and levee-channels

7.1 Calciclastic submarine fan a

Linear features are recognised in horizons H_1, H_2, and H_3, and are interpreted as erosional distributary furrows (Fig. 7k, l). These furrows suggest the presence of a turbidite system with a sediment flow direction towards the north, which created a large submarine fan. Sediment flow is funnelled by conduit *a*, widely opening from the continental slope onto the continental rise.

Channel-levee systems started to develop within the calciclastic submarine fan at the level of horizon H_3 as a result of the continuing incision of the erosional furrows (Fig. 7g, h). Channel *a* became, at this time, the major feature at this level (Fig. 7g, h). In Horizons H_4 and

506 H_5, the submarine fan becomes narrower, but with channel *a* still growing in size (Fig. 7c-f).
507 The Holocene submarine fan is no longer observed on the modern sea floor, but channel *a* has
508 grown considerably when compared with its Miocene and Pliocene counterparts (Fig. 7a, b).
509 At present, conduit *a* forms a deep, incised canyon at the shelf margin, spanning to the
510 continental rise, where it becomes a channel-levee system (Fig. 7a, b). Channel *a* is the main
511 feature on the modern sea floor with a minimum length of 56 km, continuing to the north
512 beyond the limits of the seismic data (Figs. 2 and 7a, b).

513 Morphometric data for channel *a* increase consistently as the channel evolved from
514 horizons H_4 to the seafloor (Fig. 10). Cross-sectional area and bankfull width suggest that
515 channel *a* developed over time (Fig. 10e, f). Similarly, conduit bed slope and sinuosity also
516 increase from H_4 to the sea floor. Mean slope varies from 1.6 at H_4, to 2.5 at horizon H_4, and
517 reaches a value of 3 on the sea floor, a character that proves continuing channel incision (Fig.
518 10a). Sinuosity, however, shows that as the channel evolved, its amplitude and wavelength
519 increased, reaching values of 1.04 to 1.09 (Fig. 10b-d).

520

521 **7.2 Channel b**

522 Channel *b* is first recognised in horizon H_4, developing on the continental slope (Fig. 7e,
523 f). Similarly to channel *a*, this sediment conduit grew from horizon H_4 to the sea floor (Fig. 7).
524 An aggradational stacking pattern is recognised in cross-section, suggesting a continuous
525 sediment input to channel *b* through time (Fig. 8). Area and bankfull width of the channel
526 increase upwards (Fig. 10e, f). Conduit bed slope and sinuosity do not markedly change,
527 recording mean values of 5.0-6.0 and 1.08-1.12 %, respectively (Fig. 10a, b).

528

529 **7.3 Channel c**

530 Channel *c* shows flanking levees, a character similar to the previous two channels (Figs.
531 8 and 9). Planform and cross-sectional parameters of channel *c* are comparable to channels *a*
532 and *b*; they are all aggradational, with area, bankfull width and bed slope increasing as the
533 channel evolved (Figs. 7, 8, 10). The difference between channel *a* and c is that channel *c* starts
534 as a discrete channel-levee system at the level of horizon H_2 and no submarine fan is observed
535 (Fig. 7k, l). Cross-sectional area increased from 21217.3 m^2 in horizon H_2 to 276135.7 m^2 on
536 the sea floor. Mean bankfull width values also increase from 756.7 m at horizon H_2 to 2098.1
537 m on the sea floor. Mean bed slope rises from 1.5% at H_2 to 4.7% on the seafloor. Sinuosity
538 values are similar at different stratigraphic levels, with low mean values ranging from 1.09 to
539 1.18 (Fig. 10b).

540

541 **7.4 Channels d, e and f**

542 Channels *d*, *e* and *f* are first observed on the continental slope at the level of horizon H_3
543 (Fig. 7g, h). The seismic data in this work only image the development of these conduits as
544 canyons on the continental slope, and they appear to merge into one channel near the limit
545 between the continental slope and continental rise. The funnelled channels d, e and f extend
546 beyond the limits of our seismic data (Fig. 7 g, h).

547

548 **7.5 Channel x**

549 Channel *x* is only identified in horizon H_2 (Figs. 7c, d and 8). Cross-sectional data show
550 that channel *x* did not evolve beyond horizon H_2 (Fig. 8). Its mean cross-sectional area is
551 29111.0 m^2 and its mean bankfull width is 1019.1 m. Conduit bed slope is 2.5% on average
552 and mean sinuosity is low, reaching a value of 1.1 (Fig.10).

553

554 ### 7.6 Channel y

555 Channel *y* is only observed in horizon H_1, showing a sinuous morphology that contrasts
556 with the previous channels (Fig. 7k, l). In cross-section, channel *y* is a small channel that
557 aggrades a few reflections above horizon H_1, dying out below horizon H_2 with characteristic
558 low amplitude, parallel internal reflections (Figs. 8 and 9). Mean cross-sectional area and mean
559 bankfull width are the smallest recognised when compared to the other channels, with values
560 of 6169.8 m^2 and 417.6 m, respectively. Its mean conduit bed slope is 2.18% with a high mean
561 sinuosity of 1.39 (Fig.10).

562

563 ## 8 Channel morphometric relationships

564 Channel morphometric data are here compared to power-law regressions concerning
565 submarine and fluvial channels formed in siliciclastic environments (Williams, 1986; Held,
566 2011; Lemay et al., 2020). These results confirm that calciclastic channels in the PAMA Basin
567 have a degree of similarity to their siliciclastic counterparts.

568 Width vs. depth relationships for the interpreted calciclastic channel-levee systems are
569 comparable to the siliciclastic channel models proposed by Lemay et al. (2020), in which
570 channel sizes are similar (Fig. 11 a, b). However, differences in the exponents and coefficients
571 of the power-law distribution display a less steep curve for calciclastic channels (Fig. 11a, b).
572 The latter have larger levee heights than siliciclastic channels for a given bankfull width (Fig.
573 11 a, b). Wavelength and amplitude regression data also show a less steep curve (Fig. 11c, d).
574 Thus, calciclastic channels are slightly more sinuous than siliciclastic channels, as their
575 amplitude is higher for a given wavelength (Fig. 11c, d). Data from channel *y* are particularly
576 interesting as they plot closer to the model of fluvial channels of Williams (1986), thus

577 justifying why channel *y* shows higher sinuosity values than the other calciclastic channels (*a*,
578 *b*, *c* and *x*) (Fig. 11c, d). Abandoned channels are also observed from seismic data around
579 channel *y*, revealing another similarity with meandering fluvial channels (Fig. 6e, f).

580 Bankfull width vs. meander amplitude and bankfull width vs. meander wavelength
581 relationships for calciclastic channels have low correlation values of the power-law
582 distribution, ranging from 0.04 to 0.22 (Fig. 11e-h). When compared calciclastic channel data
583 to siliciclastic channel data from Lemay et al. (2020), it is evident that this type of relationship
584 display a lower correlation (Fig. 11e-h).

585

586 # 9 Discussion

587 Oil and gas exploration on continental margins has advanced our knowledge of deep-
588 water depositional systems, as the latter contain large hydrocarbon fields (Weimer and Slatt,
589 2004; Kang et al., 2018; Lemay et al., 2020). Examples of deep-water basins with hydrocarbons
590 include the Campos Basin in Brazil, the Gulf of Mexico, the Niger Delta Basin and the Congo
591 Fan Basin in West Africa; basins that account for 70% of the global deep-water reserves to date
592 (Kang et al., 2018). Furthermore, it is important to address the evolution and depositional
593 character of deep-water systems in any offshore activity. Gravity flows in deep-water channels
594 can impact to deep-water infrastructure such as submarine cables, pipelines, or the foundations
595 of offshore wind farms (Schneider and Senders, 2010; Baker et al., 2016; Clare et al., 2017).

596 Calciclastic systems are important to understand sediment transfer off carbonate shelves
597 and isolated carbonate platforms. In the case of isolated carbonate platforms, it is relatively
598 easy to recognise pure carbonate systems in deep waters as they comprise, locally, the only
599 source of carbonate sediment. An example of this is the Glorieuses archipelago in the SW
600 Indian Ocean, in which around an isolated carbonate platform, channel-levee complexes and

turbiditic lobes were developed at water depths of 2000-3400 m (Jorry et al., 2020). In contrast, carbonate shelves have a more complex setting as they often occur adjacently to siliciclastic depositional systems. A well-documented example is the Gulf of Papua between NE Australia and S Papua New Guinea, where siliciclastic material sourced from rivers draining the Papuan Peninsula mix with carbonate deposits from the shelf and isolated carbonate platforms (Francis et al., 2008).

9.1 Mixed calciclastic-siliciclastic depositional systems in the deep and ultra-deep PAMA Basin

This work stresses the presence of a mixed calciclastic-siliciclastic depositional system on the distal continental slope in PAMA during the Miocene to Holocene, as revealed by the Travosas Formation. So far, there are no wells drilled on the distal continental slope and ultra-deep waters of PAMA to confirm the latter assumption, but based on well data from the shelf margin, we suggest a similar stratigraphy to the one observed in wells 1-MAS-9 and 1-MAS-16. In these wells, the Travosas Formation is dominated by carbonate deposits intercalated with minor siliciclastic intervals (Fig. 5). Throughout the Miocene to Holocene, the PAMA continental shelf has developed a similar environment to what we see today as reported in Soares Júnior (2002) and Soares Júnior et al. (2011). During the Miocene, the Ilha de Santana Platform was submerged forming a wide area with carbonate sediment ready to be redeposited in deep waters (Figs. 14-17 in Soares Júnior et al. 2011). Similarly, the Tiracambu mountain has sourced the inner PAMA continental shelf with siliciclastic material since the Miocene to Recent via small rivers (Fig. 1a).

The development of deep-water depositional systems is controlled by multiple factors such as basin tectonics, sea-level fluctuations, and the rates, types and sources of sediment

supply (Payros and Pujalte, 2008). According to Payros and Pujalte (2008) the most important factor generating a calciclastic submarine fan is the existence of an efficient funnelling mechanism forcing sediment gravity flows to merge downslope. Despite an initial line-source of sediment gravity flows, the physiographic profile of distally steepened ramp slopes allows the conversion of gullies and canyons to build up a point-sourced sedimentary accumulation. In our study area we can observe from horizons H_1 to the sea floor that, for the calciclastic submarine fan *a*, there is a relatively line-source of canyons, which merge together on the continental slope to create a point-source and funnel sediment coming from the shelf margin (Fig. 7). Seafloor maps are the best way to understand this process, as the whole continental slope is better imaged (Figs. 2 and 7a, b). The modern slope shows a wide array of canyons along PAMA's margin and near the border to the continental rise, some canyons merge into a single sediment conduit (Figs. 2 and 7a, b).

The way sea level affects sediment transport is distinct when comparing siliciclastic to carbonate depositional systems (Kendall and Schlager, 1981; Ma et al., 2018; Jorry et al., 2020). It is generally known that siliciclastic sediments can dominate deep-water deposition during a falling-stage or lowstand in sea level, as the inner continental shelf is exposed sub-aerially and usually connected to point-sources of sediment such as rivers, which are thus able to supply sediment directly into deep-water depocentres (Kendall and Schlager, 1981; Ma et al., 2018; Jorry et al., 2020). Submarine canyons are also commonly formed in falling-stage and lowstand periods in sea level. In contrast, carbonate basins during sea-level lowstands record a decrease in carbonate productivity as the shelf is also sub-aerially exposed and fails to export carbonate sediment into deep waters (Droxler and Schlager, 1985; Glaser and Droxler, 1993; Andresen et al., 2003; Jorry et al., 2008; Ma et al., 2018).

During sea-level transgressions and highstands, the supply of siliciclastic sediment is reduced as river deltas retrograde and the shorelines retreat landward (Droxler and Schlager,

650 1985; Glaser and Droxler, 1993; Andresen et al., 2003; Jorry et al., 2008; Ma et al., 2018). Sea-
651 level highstands are stages in which organic productivity increases on carbonate shelves
652 allowing for their lateral expansion. The accompanying increase in slope instability has
653 demonstrated that this stage promotes the transport of calciclastic sediment into deep-water
654 basins (Droxler and Schlager, 1985; Glaser and Droxler, 1993; Andresen et al., 2003; Jorry et
655 al., 2008; Ma et al., 2018). Ramp aprons, calciclastic submarine fans, channel-levee systems
656 and elongate lobes of mud-rich calciturbidites are characteristic of transgressive and highstand
657 periods in sea level (Droxler and Schlager, 1985; Glaser and Droxler, 1993; Andresen et al.,
658 2003; Jorry et al., 2008; Ma et al., 2018). As an example, Tournadour et al. (2017) explain that
659 submarine canyons in the Bahamas are related to slope failure followed by different stages of
660 regressive erosion on isolated carbonate platforms.

661 Recent studies have proven that sea-level lowstand periods contribute to exporting
662 calciclastic material into deep-water basins. Jorry et al. (2020) demonstrate that certain
663 topographic features on the shelf break and leeward slopes play an important role on carbonate
664 shelves by storing sediment that is initially shed during sea-level highstands to be later re-
665 mobilised during lowstands as calciturbidite deposits. This suggests that some calciturbidites
666 behave like siliciclastic turbidites. Examples include the channel-levee complexes of the
667 Glorieuses archipelago, SW Indian Ocean (Jorry et al., 2020), and calciturbidites in the
668 Northern Nicaragua Rise (Reijmer and Andresen, 2007), the Exuma Sounds, Bahamas
669 (Reijmer et al., 2012, 2015b), and deposited along the Great Barrier Reef (Puga-Bernabéu et
670 al., 2014). Furthermore, Payros and Pujalte (2008) suggest that in carbonate ramps with no
671 rimmed platforms, such as in PAMA, shallow-water sediment production is generally not
672 interrupted in distally steepened ramps during lowstands because productive zones in shallow
673 waters can shift basinwards (Wright and Burchette, 1998; Payros and Pujalte, 2008).

674 The data in this work reveal a complex scenario when considering the development of
675 calciclastic submarine fans and channel-levee systems in the PAMA Basin during the Miocene
676 to Holocene. The whole Equatorial Margin of Brazil experienced similar conditions, therefore
677 it is common in the literature to correlate observations from adjacent basins (Soares et al., 2007;
678 Piovesan, 2008; Rossetti et al., 2013). Sea-level curves for the PAMA Basin can be
679 extrapolated from outcrop observations of the Pirabas and Barreiras formations (Rossetti et al.,
680 2013) (Fig. 4). The study from Rossetti et al. (2013) concluded that two major marine
681 transgressive episodes occurred in Equatorial Brazil, one in the Oligocene-Miocene and the
682 other in the early-middle Miocene (Fig. 4). Both events correlate with sea-level highstands
683 recorded in other South American basins and also worldwide (Rossetti et al., 2013). Oligocene-
684 Miocene marine deposits are represented by the Pirabas Formation, which accumulated at a
685 time when a rise in sea level was recorded in several parts of the world. Rossetti et al. (2013)
686 also reported a sea-level drop immediately before the start of the late Miocene with no
687 subsequent transgressions being recorded, at least until the late Quaternary. This drop in sea-
688 level is recognised by the development of a regional unconformity and formation of a lateritic
689 soil at the top of the Barreiras Formation.

690 During the late Oligocene-lower Miocene (Sequence E80-N10), there was a major
691 transgressive event covering all the Brazilian Equatorial Margin, associated with the Pirabas
692 Sea, leading to an expansion of the carbonate shelf (Soares et al., 2007). These observations
693 coincide with the transgressive episode reported in Rossetti et al. (2013) (Fig. 4). Upper
694 Oligocene-lower Miocene strata are considered part of Unit 1 in this work. At the top of Unit
695 1 (horizon H_1), a sinuous channel (channel *y*) is recognised as well as several linear furrows
696 forming a calciclastic submarine fan funnelled by sediment conduit *a* (Fig. 7k, l). Furrows can
697 be related to turbidity flows similar to those recorded in the Little Bahama Bank (Tournadour
698 et al., 2017), and cover a large area with no developed channels at this time (Fig. 7k, l). This

699 interpretation agree with the model proposed by Payros and Pujalte (2008) in which the major
700 transport of calciclastic deposits occur during sea-level highstands in the form of turbidity
701 flows.

702 The shoreline transgression during the Early Miocene, to a position far from the shelf
703 edge restricted the influx of siliciclastic sediment onto the continental shelf, suggesting that
704 carbonate sediment was the predominant type feeding PAMA's deep-water basins at that time.
705 As described earlier, channel *y* is only observed in Horizon H_1 and does not continue upwards
706 in Unit 1. Our interpretation is that, unlike the calciclastic submarine fan *a*, there was no
707 effective funnelling system feeding channel *y* above horizon H_1, leading to its abandonment
708 (Figs.7-9).

709 Based on the data from Soares et al. (2007) and Rossetti et al. (2013), we interpret the
710 middle Miocene (Unit 2) as a falling stage in sea level. Soares et al. (2007) suggested that there
711 is an unconformity in well and seismic data correlating with a marked sea level drop that
712 occurred in PAMA before the late Miocene (Rossetti et al., 2013). In the study area, Horizon
713 H_3 is interpreted being the unconformity described in Soares et al. (2007), separating moderate-
714 to-high-amplitude seismic reflections from low-amplitude strata above (Figs. 3b and 9). At the
715 level of horizon H_3, tributary channel-levee systems were first developed within the calciclastic
716 submarine fan, with channel *a* constituting the main sediment conduit (Fig. 7g, h). The
717 development of tributary channels suggests that sediment supply was significant at the time,
718 although relatively smaller in volume when compared to strata at the level of horizon H_1. This
719 interpretation is also corroborated by a decrease in size of the calciclastic submarine fan in
720 younger strata, until the fan disappears near the modern seafloor. Conversely, a considerable
721 growth of channel *a* is still recorded within the submarine fan until one reaches the modern sea
722 floor, where the channel becomes the predominant feature (Figs. 2, 7 and 10).

723 Channel *c* started developing at the level of horizon H_2 (Fig. 7i, j). This channel is
724 important as it shows a constant aggradation towards younger strata (Fig. 8). The aggradation
725 of channel *c,* accompanying its lateral migration, suggests that sediment input to the channel
726 was constant regardless of any relative changes in sea level; geomorphic parameters such as
727 cross-sectional area and bankfull width reveal that channel *c* continued to grow over time
728 (Fig.10). Horizon H_3, correlating with the relative drop in the sea level documented in Soares
729 et al. (2007), also reveals that channel *c* did not stop developing at this time, and its geometry
730 remained constant. In addition, Soares et al. (2007) suggest that at the end of the late Miocene
731 and Pliocene (Sequence N40-N50), both the carbonate shelf and associated coastal depositional
732 systems prograded over the PAMA Basin, a character justifying why channel *c* remained active
733 during the deposition of Unit 3.

734 The continuous development of channel *c* during successive sea-level high- and
735 lowstands, together with its constant sinuosity values through time, prove that calciclastic
736 depositional systems are not primarily controlled by sea-level change, as also suggested in
737 Payros and Pujalte (2008). A possible explanation to the observed aggradation of channel *c*
738 through multiple fluctuations in sea level is the existence of an efficient funnelling mechanism
739 on the continental slope (Fig. 7). Additionally, as described in Jorry et al. (2020), calciclastic
740 sediments can be shed to deep-water systems not just during sea-level highstands, but also
741 during lowstands. Calciclastic sediments might have accumulated on terraces at the slope, to
742 be later redeposited during falling-stages and lowstands in sea-level (Fig. 7).

743

744 **9.2 Geomorphic characteristics of carbonate deep-water levee-channels**

745 Geomorphic analyses of deep-water channel-levee systems fed by siliciclastic sediment
746 have been previously documented in Lemay et al. (2020) and compared to fluvial channels. It

747 was recognised that submarine channels are one to two orders of magnitude wider and deeper
748 than fluvial channels, with the latter being more sinuous than submarine channels (Lemay et
749 al., 2020). In this work, we determine how similar calciclastic levee-channels are in comparison
750 to their siliciclastic counterparts.

751 Based on our results and comparison with published power-law relationships, we can
752 confirm that bankfull width vs. depth relationships of calciclastic channels in PAMA are
753 similar and comparable to siliciclastic channels (Fig. 11a, b). However, calciclastic channels
754 are deeper than siliciclastic channels for a given bankfull width (Fig. 11a, b). Calciclastic
755 channels also appear to be slightly more sinuous than siliciclastic channels as the regression
756 curve between meander amplitude and wavelength is less steep (Fig. 11c, d). Sinuosity values
757 recorded in channel *y* approaches the sinuosity of meandering fluvial channels, marking a
758 distinction with other channels (Fig. 11c). In fact, three different types of calciclastic sediment
759 conduits have been observed in the PAMA Basin: i) Type 1, which are channel-levee systems
760 related to calciclastic submarine fans (channel *a*), ii) Type 2, comprising low sinuosity channel-
761 levee systems *b, c* and *x*, and iii) Type 3, which is represented by highly sinuous channel *y*
762 (Fig.12).

763

764 ***9.2.1 Type 1 – channels related to calciclastic submarine fans***

765 The early stages of this type of channel are associated with erosive turbidity currents
766 developing furrows within a calciclastic submarine fan (Fig. 12a). These furrows are
767 recognised in cross-sectional data and on key seismic reflectors as small spikes, which mark
768 the loci of incision of erosive turbidity currents (Fig. 12b). As the incision of the furrows
769 continues, a channel-levee system may develop, such as channel *a* (Fig. 12c, d). This type of

channel is characterised by its low sinuosity, and by presenting geomorphic features similar to its siliciclastic counterparts (Fig. 11).

9.2.2 Type 2 – low sinuosity, aggradational channels

Type 2 channels record low sinuosity values, usually less than 1.3 (Figs.10 and 12e). Type 2 channels are not associated with calciclastic submarine fans and originate due to the funnelling of sediment from upper slope canyons to form, downslope, a well-defined sediment conduit (Fig. 12h). They start as small channels with high-amplitude internal reflections (Fig. 12f). Due to the characteristic mixing of carbonate and siliciclastic deposits through multiple episodes of sea-level rise and fall, aggradational features are observed in their interior, leading to the generation of large channel-levee systems (Fig. 12g, h).

9.2.3 Type 3 – high-sinuosity channels

The high sinuosity (average of 1.4) of Type 3 channels is comparable to fluvial channels (Figs. 10b, 11b and 12i). Channel *y* shows features such as abandoned channels that suggest a change in its flow direction (Fig. 12i, j). In contrast to the previous low sinuosity channels (Type 2), the cross-sectional area of Type 3 channels is considerably smaller (Fig. 10). This type of channel does not aggrade over time, implying that sediment sources were episodic and not continuous.

10 Conclusions

The main conclusions concerning the deep and ultra-deep mixed calciclastic-siliciclastic depositional systems of the Miocene-Holocene PAMA Basin can be summarised as follows:

a) We postulate that a portion of the Miocene-Holocene strata of the Travosas Formation comprises a mixed calciclastic-siliciclastic depositional system recording a dominant carbonate input from the continental shelf. A calciclastic submarine fan and channel-levee systems are identified within deep and ultra-deep waters of the PAMA Basin.

b) Multispectral satellite data point out to a dynamic sediment transport on a mixed calciclastic-siliciclastic carbonate shelf. The PAMA continental shelf is divided into a mixed carbonate-siliciclastic zone in its inner part, and an autochthonous carbonate zone in its middle and outer zones.

c) Geomorphologic relationships of the PAMA calciclastic channel-levee systems show similarities with modern siliciclastic submarine channel models previously published by Lemay et al. (2020).

d) The formation of a large calciclastic submarine fan in the lower Miocene correlates with a period of progradation and lateral growth of the carbonate shelf during a sea-level rise. Erosional furrows are characteristic of distal fans, and comprise an effective funnelling mechanism for younger channels forming on the continental slope.

e) Three different types of deep-water depositional systems are recognised in the PAMA Basin: channels related to calciclastic submarine fans (Type 1), low sinuosity-aggradational channels (Type 2), and high sinuosity channels (Type 3).

f) Channels related to calciclastic submarine fans (Type 1), such as channel *a*, were initiated by the action of highstand turbidity flows. The continuous erosive turbidite flows led to an increase in the funnelling of sediment, developing a large channel-levee system.

g) Low-sinuosity channels (Type 2) are not associated with calciclastic submarine fans, are aggradational, and appear to develop through time regardless of any relative sea-level change. This can be explained by the accumulation of sediment in topographic

features, such as terraces on the continental slope, which is later redeposited during sea-level lowstands. Furthermore, the presence of a steepened ramp on the PAMA continental shelf provides a continuous supply of carbonate material during sea-level lowstands as the productive zone shifts basinwards.

h) Highly sinuous channels (Type 3) are characterised by their small cross-sectional area, showing a bankfull wavelength vs. amplitude relationship, and sinuosity values, that are similar to fluvial channels.

11 Acknowledgements

The work contained in this paper is part of a PhD research supported by the Mexican National Council of Science and Technology (CONACYT) and the hydrocarbon Secretariat of Energy (SENER). Polarcus is acknowledged to provide the Pará-Maranhão 3D seismic volume as well as Schlumberger Petrel® and ESRI ArcGIS® for granting academic licenses to Cardiff's 3D Seismic Lab. The authors acknowledge the Brazilian National Agency of Petroleum, Natural Gas and Biofuels (ANP) for the well data provided. We thank Martin Lemay for sharing the Python scripts used for the channel planform measurements as well as the data for modern siliciclastic sediment conduits. We also would like to thank Basin Research Editor, Peter Burgess and reviewers Lorena Moscardelli and Xavier Janson for their useful and constructive comments.

12 References

Aguilera, O., Oliveira de Araújo, O.M., Hendy, A., Nogueira, A.A.E., Nogueira, A.C.R., Maurity, C.W., Kutter, V.T., Martins, M.V.A., Coletti, G., Dias, B.B., da Silva-Caminha, S.A.F., Jaramillo, C., Bencomo, K., Lopes, R.T., 2020. Palaeontological framework from Pirabas Formation (North Brazil) used as potential model for equatorial carbonate platform. Marine Micropaleontology 154, 101813.

Almeida, N.M. De, Alves, T.M., Filho, F.N., Souza, A.C.B., Oliveira, K.M.L., Barbosa, T.H.S., 2020. A three-dimensional (3D) structural model for an oil-producing basin of the Brazilian Equatorial margin. Marine and Petroleum Geology.

Almeida, N., Alves, T., Filho, N., Freire, S., de Souza, C., Leopoldino, K., Normando, M., Barbosa, T., 2018. Tectono-sedimentary evolution and petroleum system of a new deep-water exploration frontier: Mundaú sub-basin Equatorial Brazil. AAPG Bulletin 0, 20.

Alves, T., Fetter, M., Busby, C., Gontijo, R., Cunha, T.A., Mattos, N.H., 2020. A tectono-stratigraphic review of continental breakup on intraplate continental margins and its impact on resultant hydrocarbon systems., Marine and Petroleum Geology.

Alves, T.M., Abreu Cunha, T., 2018. A phase of transient subsidence, sediment bypass and deposition of regressive–transgressive cycles during the breakup of Iberia and Newfoundland. Earth and Planetary Science Letters 484, 168–183.

Andresen, N., Reijmer, J.J.G., Droxler, A.W., 2003. Timing and distribution of calciturbidites around a deeply submerged carbonate platform in a seismically active setting (Pedro Bank, Northern Nicaragua Rise, Caribbean Sea). International Journal of Earth Sciences 92, 573–592.

Aquino da Silva, A.G., Amaro, V.E., Stattegger, K., Schwarzer, K., Vital, H., Heise, B., 2015.

863 Spectral calibration of CBERS 2B multispectral satellite images to assess suspended
864 sediment concentration. ISPRS Journal of Photogrammetry and Remote Sensing 104, 53–
865 62.

866 Back, S., Reuning, L., 2015. Channels in Carbonate Environments: 3-D-Seismic
867 Characteristics Extracted From the Sedimentary Record. AAPG Annual Convention and
868 Exhibition, Denver, Co.

869 Baker, E., Gaill, F., Karageorgis, A., Lamarche, G., Narayanaswamy, B., Parr, J.,
870 Raharimananirina, C., Santos, R., Sharma, R., Tuhumwire, J., 2016. Offshore mining
871 industries. In: (UN), U.N. (Ed.), The First Global Integrated Marine Assessment; World
872 Ocean Assessment I. New York, NY, USA.

873 Betzler, C., Lindhorst, S., Eberli, G.P., Lüdmann, T., Möbius, J., Ludwig, J., Schutter, I.,
874 Wunsch, M., Reijmer, J.J.G., Hübscher, C., 2014. Periplatform drift: The combined result
875 of contour current and off-bank transport along carbonate platforms. Geology 42, 871–
876 874.

877 Betzler, C., Reijmer, J.J.G., Bernetà, K., Eberlià, G.P., Anselmetti, F.S., 1999. Sedimentary
878 patterns and geometries of the Bahamian outer carbonate ramp (Miocene±Lower
879 Pliocene, Great Bahama Bank). Sedimentology 46.

880 Bornhold, B.D., Pilkey, O.H., 1971. Bioclastic turbidite sedimentation in Columbus Basin,
881 Bahamas. Bulletin of the Geological Society of America 82, 1341–1354.

882 Braga, J.C., Martin, J.M., Wood, J.L., 2001. Submarine lobes and feeder channels of
883 redeposited, temperate carbonate and mixed siliciclastic-carbonate platform deposits
884 (Vera Basin, Almerõ Âa, southern Spain).

885 Brandão, J., Feijó, F.J., 1994. Bacia do Pará-Maranhão. Boletim de Geociências Da

886 PETROBRÁS 8, 101–102.

887 Catuneanu, O., 2006. Principles of sequence stratigraphy. Elsevier.

888 Chiarella, D., Longhitano, S.G., Tropeano, M., 2017. Types of mixing and heterogeneities in
889 siliciclastic-carbonate sediments. Marine and Petroleum Geology 88, 617–627.

890 Clare, M.A., Vardy, M.E., Cartigny, M.J.B., Talling, P.J., Himsworth, M.D., Dix, J.K., Harris,
891 J.M., Whitehouse, R.J.S., Belal, M., 2017. Direct monitoring of active geohazards:
892 Emerging geophysical tools for deep-water assessments. Near Surface Geophysics 15,
893 427–444.

894 Coniglio, M., Dix, G.R., 1992. Carbonate Slopes. In: Walker, R.G., James, N.P. (Eds.), Facies
895 Models–Response to Sea-Level Change. Geological Association of Canada, St. John's
896 Newfoundland.

897 Counts, J.W., Jorry, S.J., Vazquez Riveiros, N., Jouet, G., Giraudeau, J., Cheron, S., Boissier,
898 A., Miramontes, E., 2019. A Late Quaternary record of highstand shedding from an
899 isolated carbonate platform (Juan de Nova, southern Indian Ocean). The Depositional
900 Record 5, 540–557.

901 Crevello, P.D., Schlager, W., 1980. Carbonate debris sheets and turbidites, Exuma Sound,
902 Bahamas. Journal of Sedimentary Petrology 50, 1121–1148.

903 Cross, T.A., Lessenger, M.A., 1988. Seismic Stratigraphy. Annual Review of Earth and
904 Planetary Sciences 16, 319–354.

905 Da Silva, B., Ribeiro, H.J.P.S., 2018. Exploratory plays of Pará-Maranhão and Barreirinhas
906 basins in deep and ultra-deep waters, Brazilian Equatorial Margin. Brazilian Journal of
907 Geology 48, 485–502.

908 Da Silva, C.P., 2007. Estudo Sobre Foraminíferos e Radiolários do Cretáceo, Bacia Pará-

909 Maranhão, Margem Equatorial Brasileira. Universidade Federal do Rio Grande do Sul.

910 de Morais, J.O., Ximenes Neto, A.R., Pessoa, P.R.S., de Souza Pinheiro, L., 2019.
911 Morphological and sedimentary patterns of a semi-arid shelf, Northeast Brazil. Geo-
912 Marine Letters 40, 1–8.

913 De Souza, V., 2006. Radiolários Do Cretáceo Médio Das Bacias Do Pará-Maranhão E
914 Barreirinhas, Margem Equatorial Brasileira Vladimir. Universidade Federal do Rio
915 Grande do Sul.

916 Dias, F.J.S., Castro, B.M., Lacerda, L.D., 2013. Continental shelf water masses off the
917 Jaguaribe River (4S), northeastern Brazil. Continental Shelf Research 66, 123–135.

918 Ditty, P.S., Harmon, C.J., Pilkey, O.H., Ball, M.M., Richardson, E.S., 1977. Mixed
919 terrigenous-Carbonate sedimentation in the Hispaniola-Caicos turbidite basin. Marine
920 Geology 24, 1–20.

921 Droxler, A.W., Schlager, W., 1985. Glacial versus interglacial sedimentation rates and turbidite
922 frequency in the Bahamas. Geology 13, 799–802.

923 Dunlap, D., Janson, X., Sanchez Phelps, C., Covault, J., 2018. Carbonate Channel-Levee
924 Systems Influenced by Mass-Transport Complexes, Browse Basin, Western Australia.
925 AAPG ACE 2018.

926 Eberli, G.P., Anselmetti, F.S., Betzler, C., Van Konijnenburg, J.H., Bernoulli, D., 2005.
927 Carbonate platform to basin transitions on seismic data and in outcrops: Great Bahama
928 Bank and the Maiella Platform margin, Italy. AAPG Memoir 207–250.

929 Eberli, G.P., Swart, P.K., McNeill, D.F., Kenter, J.A.M., Anselmetti, F.S., Melim, L.A.,
930 Ginsburg, R.N., 1997. A synopsis of the Bahamas Drilling Project: results from two deep
931 core borings drilled on the Great Bahama Bank. In: Marin, J.A. (Ed.), Proceedings of the

932 Ocean Drilling Program, Initial Reports. Ocean Drilling Program, Texas A&M
933 University, 23–41.

934 Fabianovicz, R., 2013. Pará-Maranhão Basin. Brasil 11th Round - Oil & Gas Bidding Rounds.
935 National Agency of Petroleum, Natural Gas and Biofuels, Rio de Janeiro.

936 Figueiredo, J.D.J.P. De, Zalán, P.V., Soares, E.F., 2007. Bacia da Foz do Amazonas. Boletim
937 de Geociencias - Petrobras 15, 299–309.

938 Francis, J.M., Daniell, J.J., Droxler, A.W., Dickens, G.R., Bentley, S.J., Peterson, L.C.,
939 Opdyke, B.N., Beaufort, L., 2008. Deep water geomorphology of the mixed siliciclastic-
940 carbonate system, Gulf of Papua. Journal of Geophysical Research: Earth Surface 113, 1–
941 22.

942 Gallagher, S.J., Smith, A.J., Jonasson, K., Wallace, M.W., Holdgate, G.R., Daniels, J., Taylor,
943 D., 2001. The miocene palaeoenvironmental and palaeoceanographic evolution of the
944 gippsland basin, southeast australia: A record of southern ocean change.
945 Palaeogeography, Palaeoclimatology, Palaeoecology 172, 53–80.

946 Gee, M.J.R., Gawthorpe, R.L., Bakke, K., Friedmann, S.J., 2007. Seismic geomorphology and
947 evolution of submarine channels from the Angolan continental margin. Journal of
948 Sedimentary Research 77, 433–446.

949 Glaser, K.S., Droxler, A.W., 1993. Controls and Development of Late Quaternary Periplatform
950 Carbonate Stratigraphy in Walton Basin (Northeastern Nicaragua Rise, Caribbean Sea).
951 Paleoceanography 8, 243–274.

952 Gradstein, F.M., Ogg, J.G., Smith, A.G., 2005. A geologic time scale 2004, A Geologic Time
953 Scale 2004. Cambridge University Press.

954 Hedley, J.D., Roelfsema, C., Brando, V., Giardino, C., Kutser, T., Phinn, S., Mumby, P.J.,

955 Barrilero, O., Laporte, J., Koetz, B., 2018. Coral reef applications of Sentinel-2: Coverage,
956 characteristics, bathymetry and benthic mapping with comparison to Landsat 8. Remote
957 Sensing of Environment 216, 598–614.

958 Held, A., 2011. Apport de la paléohydrologie dans la quantification des rôles respectifs du
959 climat et de la tectonique des systèmes fluviatiles méandriformes fossiles : application à
960 des systèmes oligo-miocènes d ' Europe occidentale To cite this version : HAL Id : paste,
961 http://www.theses.fr. Paris, ENMP.

962 Henry, S., Kumar, N., Danforth, A., Nuttall, P., Venkatraman, S., 2011. Ghana-Sierra Leone
963 Lookalike Plays in Northern Brazil. GeoExPro 8, 36–41.

964 James, N.P., Mountjoy, E.W., 1983. Shelf-slope break in fossil carbonate platforms: an
965 overview. In: Stanley, D.J., Moore, G.T. (Eds.), The Shelfbreak: Critical Interface on
966 Continental Margins. SEPM Special Publication, 33. SEPM Society for Sedimentary
967 Geology, 189–206.

968 Janson, X., Dunlap, D., Zeng, L., Sanchez Phelps, C., Covault, J., 2018. Carbonate Shelf to
969 Basin Architecture and Slope Seismic Geomorphology, Lower Miocene, Browse Basin,
970 Northwest Shelf of Australia. AAPG ACE 2018.

971 Jorry, S.J., Droxler, A.W., Mallarino, G., Dickens, G.R., Bentley, S.J., Beaufort, L., Peterson,
972 L.C., Opdyke, B.N., 2008. Bundled turbidite deposition in the central Pandora Trough
973 (Gulf of Papua) since Last Glacial Maximum: Linking sediment nature and accumulation
974 to sea level fluctuations at millennial timescale. Journal of Geophysical Research: Earth
975 Surface 113, 1–15.

976 Jorry, S.J., Jouet, G., Edinger, E.N., Toucanne, S., Counts, J.W., Miramontes, E., Courgeon,
977 S., Riveiros, N.V., Le Roy, P., Camoin, G.F., 2020. From platform top to adjacent deep
978 sea: New source-to-sink insights into carbonate sediment production and transfer in the

979 SW Indian Ocean (Glorieuses archipelago). Marine Geology.

980 Kang, H., Meng, J., Cheng, T., Jia, H., Bai, B., Li, M., 2018. Characteristics of deep water
981 depositional system in Campos basin, Brazil. Petroleum Exploration and Development
982 45, 99–110.

983 Kendall, C.G.S.C., Schlager, W., 1981. Carbonates and relative changes in sea level. Marine
984 Geology 44, 181–212.

985 Kenter, J.A.M., 1990. Carbonate platform flanks: slope angle and sediment fabric.
986 Sedimentology 37, 777–794.

987 Lemay, M., Grimaud, J.L., Cojan, I., Rivoirard, J., Ors, F., 2020. Geomorphic variability of
988 submarine channelized systems along continental margins: Comparison with fluvial
989 meandering channels. Marine and Petroleum Geology 115, 104295.

990 Ma, B., Wu, S., Mi, L., Lüdmann, T., Gao, J., Gao, W., 2018. Mixed Carbonate-Siliciclastic
991 Deposits in a Channel Complex in the Northern South China Sea. Journal of Earth Science
992 29, 707–720.

993 Milliman, J.D., 1993. Production and accumulation of calcium carbonate in the ocean: budget
994 of a nonsteady state. Global Biogeochemical Cycles 7, 927–957.

995 Moscardelli, L., Ochoa, J., Hunt, I., Zahm, L., 2019. Mixed siliciclastic–carbonate systems and
996 their impact for the development of deep-water turbidites in continental margins: A case
997 study from the Late Jurassic to Early Cretaceous Shelburne subbasin in offshore Nova
998 Scotia. AAPG Bulletin 103, 2487–2520.

999 Mulder, T., Ducassou, E., Gillet, H., Hanquiez, V., Principaud, M., Chabaud, L., Eberli, G.P.,
1000 Kindler, P., Billeaud, I., Gonthier, E., Fournier, F., Leonide, P., Borgomano, J., 2014. First
1001 Discovery of Channel-Levee Complexes In A Modern Deep-Water Carbonate Slope

1002 Environment. Journal of Sedimentary Research 84, 1139–1146.

1003 Mulder, T., Ducassou, E., Gillet, H., Hanquiez, V., Tournadour, E., Combes, J., Eberli, G.P.,
1004 Kindler, P., Gonthier, E., Conesa, G., Robin, C., Sianipar, R., Reijmer, J.J.G., François,
1005 A., 2012. Canyon morphology on a modern carbonate slope of the bahamas: Evidence of
1006 regional tectonic tilting. Geology 40, 771–774.

1007 Nemčok, M., Henk, A., Allen, R., Sikora, P.J., Stuart, C., 2013. Continental break-up along
1008 strike-slip fault zones; observations from the equatorial Atlantic. Geological Society
1009 Special Publication 369, 537–556.

1010 Oliveira, M.J.R., Santarem, P., Moraes, A., Zalán, P. V., Caldeira, J.L., Tanaka, A., Trosdtorf,
1011 I., 2012. Linked extensional-compressional tectonics in gravitational systems in the
1012 equatorial margin of Brazil. AAPG Memoir 159–178.

1013 Payros, A., Pujalte, V., 2008. Calciclastic submarine fans: An integrated overview., Earth-
1014 Science Reviews.

1015 Payros, A., Pujalte, V., Orue-Etxebarria, X., 2007. A point-sourced calciclastic submarine fan
1016 complex (Eocene Anotz Formation, western Pyrenees): facies architecture, evolution and
1017 controlling factors. Sedimentology 54, 137–168.

1018 Pettingill, H.S., 2006. Global Overview of Deepwater Exploration and Production. In: Weimer,
1019 P., Slatt, R.M., Bouroullec, R., Fillon, R., Pettingill, H., Pranter, M., Tari, G. (Eds.),
1020 Introduction to the Petroleum Geology of Deepwater Setting. American Association of
1021 Petroleum Geologists (AAPG).

1022 Piovesan, E.K., 2008. Ostracodes Cretáceos (Turoniano-Maastrichtiano) Da Bacia Do Pará-
1023 Maranhão: Aspectos Taxonômicos, Paleoecológicos E Paleobiogeográficos.
1024 Universidade do Vale do Rio dos Sinos.

1025 Playton, T.E., Janson, X., Kerans, C., 2010. Carbonate Slopes. In: James, N., Dalrymple, R.W.
1026 (Eds.), Facies Models 4. Geological Association of Canada, St. Johns, Newfoundland,
1027 449–476.

1028 Puga-Bernabéu, Á., Webster, J.M., Beaman, R.J., Reimer, P.J., Renema, W., 2014. Filling the
1029 gap: A 60ky record of mixed carbonate-siliciclastic turbidite deposition from the Great
1030 Barrier Reef. Marine and Petroleum Geology 50, 40–50.

1031 Rankey, E.C., 2017. Seismic architecture and seismic geomorphology of heterozoan
1032 carbonates: Eocene-Oligocene, Browse Basin, Northwest Shelf, Australia. Marine and
1033 Petroleum Geology 82, 424–443.

1034 Ravenne, C., Vially, R., Francaise, C., Valery, P., 1985. Deep Clastic Carbonate Deposits of
1035 the Bahamas — Comparison With Mesozoic Outcrops of the Vercors and Vocontian
1036 Trough.

1037 Reijmer, J.J.G., Andresen, N., 2007. Mineralogy and grain size variations along two carbonate
1038 margin-to-basin transects (Pedro Bank, Northern Nicaragua Rise). Sedimentary Geology
1039 198, 327–350.

1040 Reijmer, J.J.G., Mulder, T., Borgomano, J., 2015a. Carbonate slopes and gravity deposits.
1041 Sedimentary Geology 317, 1–8.

1042 Reijmer, J.J.G., Palmieri, P., Groen, R., 2012. Compositional variations in calciturbidites and
1043 calcidebrites in response to sea-level fluctuations (Exuma Sound, Bahamas). Facies 58,
1044 493–507.

1045 Reijmer, J.J.G., Palmieri, P., Groen, R., Floquet, M., 2015b. Calciturbidites and calcidebrites:
1046 Sea-level variations or tectonic processes? Sedimentary Geology 317, 53–70.

1047 Rinke-Hardekopf, L., Reuning, L., Bourget, J., Back, S., 2018. Syn-sedimentary deformation

as a mechanism for the initiation of submarine gullies on a carbonate platform to slope transition, Browse Basin, Australian North West Shelf. Marine and Petroleum Geology 91, 622–630.

Rossetti, D.F., Bezerra, F.H.R., Dominguez, J.M.L., 2013. Late oligocene-miocene transgressions along the equatorial and eastern margins of brazil. Earth-Science Reviews 123, 87–112.

Savitzky, A., Golay, M.J.E., 1964. Smoothing and differentiation of data by simplified least squares procedures. Analytical Chemistry 36, 1627–1639.

Schneider, J.A., Senders, M., 2010. Foundation design: A comparison of oil and gas platforms with offshore wind turbines. Marine Technology Society Journal 44, 32–51.

Soares, D.M., Alves, T.M., Terrinha, P., 2012. The breakup sequence and associated lithospheric breakup surface: Their significance in the context of rifted continental margins (West Iberia and Newfoundland margins, North Atlantic). Earth and Planetary Science Letters 355–356, 311–326.

Soares, E.F., Zalán, P.V., Figueiredo, J.J.P., Trosdtorf Jr, I., 2007. Bacia do Pará-Maranhão. Boletim de Geociências Da Petrobras 15, 321–330.

Soares Júnior, A.V., 2002. Paleografia e evolução da paisagem do nordeste do estado do Pará e noroeste do Maranhão: cretáceo ao holoceno, Arsyad, Azhar,. Universidade Federal do Pará.

Soares Júnior, A.V., Hasui, Y., Costa, J.B.S., Machado, F.B., 2011. Evolução do rifteamento e paleogeografia da margem Atlântica Equatorial do Brasil: Triássico ao Holoceno. Geociencias 30, 669–692.

Sylvester, Z., Pirmez, C., 2017. Latitudinal changes in the morphology of submarine channels:

1071 Reevaluating the evidence for the influence of the coriolis force. SEPM Special
1072 Publications 108, 82–92.

1073 Tesch, P., Reece, R.S., Pope, M.C., Markello, J.R., 2018. Quantification of architectural
1074 variability and controls in an Upper Oligocene to Lower Miocene carbonate ramp, Browse
1075 Basin, Australia. Marine and Petroleum Geology 91, 432–454.

1076 Tournadour, E., Mulder, T., Borgomano, J., Gillet, H., Chabaud, L., Ducassou, E., Hanquiez,
1077 V., Etienne, S., 2017. Submarine canyon morphologies and evolution in modern carbonate
1078 settings: The northern slope of Little Bahama Bank, Bahamas. Marine Geology 391, 76–
1079 97.

1080 Trosdtorf Junior, I., Zalán, P.V., Figueiredo, J. de J.P. De, Soares, E.F., 2007. Bacia de
1081 Barreirinhas. Boletim de Geociencias - Petrobras 15, 331–339.

1082 Weimer, P., Slatt, R.M., 2004. Deepwater Reservoir Elements: Channels and their Sedimentary
1083 Fill. In: Weimer, P., Slatt, R. (Eds.), Petroleum Systems of Deepwater Settings. Society
1084 of Exploration Geophysicists and European Association of Geoscientists and Engineers.

1085 Williams, G.P., 1986. River meanders and channel size. Journal of Hydrology 88, 147–164.

1086 Wright, V.P., Burchette, T.P., 1998. Carbonate ramps: An introduction. Geological Society
1087 Special Publication 149, 1–5.

1088 Wunsch, M., Betzler, C., Lindhorst, S., Lüudmann, T., Eberli, G.P., 2017. Sedimentary
1089 dynamics along carbonate slopes (Bahamas archipelago). Sedimentology 64, 631–657.

1090 Zalán, P.V., 2015. Re-Interpretation of an Ultra-Deep Seismic Section in the Para-Maranhao
1091 Basin - Implications for the Petroleum Potential of the Ultra-Deep Waters. OTC Brasil
1092 2015: The Atlantic: From East to West - An Ocean of Innovation. 662–672.

1093 Zalán, P.V., 2001. Growth Folding in Gravitational Fold-and-Thrust Belts in the Deep Waters

of the Equatorial Atlantic, Northeastern Brazil. Seventh International Congress of the Brazilian Geophysical Society. AAPG Datapages/Search and Discovery.

Zeng, L.Y., 2020. Seismic-based geomorphology of a mixed carbonate siliciclastic shelf-to-basin submarine drainage system , Miocene , Browse Basin , Northwest Shelf of Australia APPROVED BY SUPERVISING COMMITTEE : The University of Texas at Austin.

13 Figures

FIGURE 1

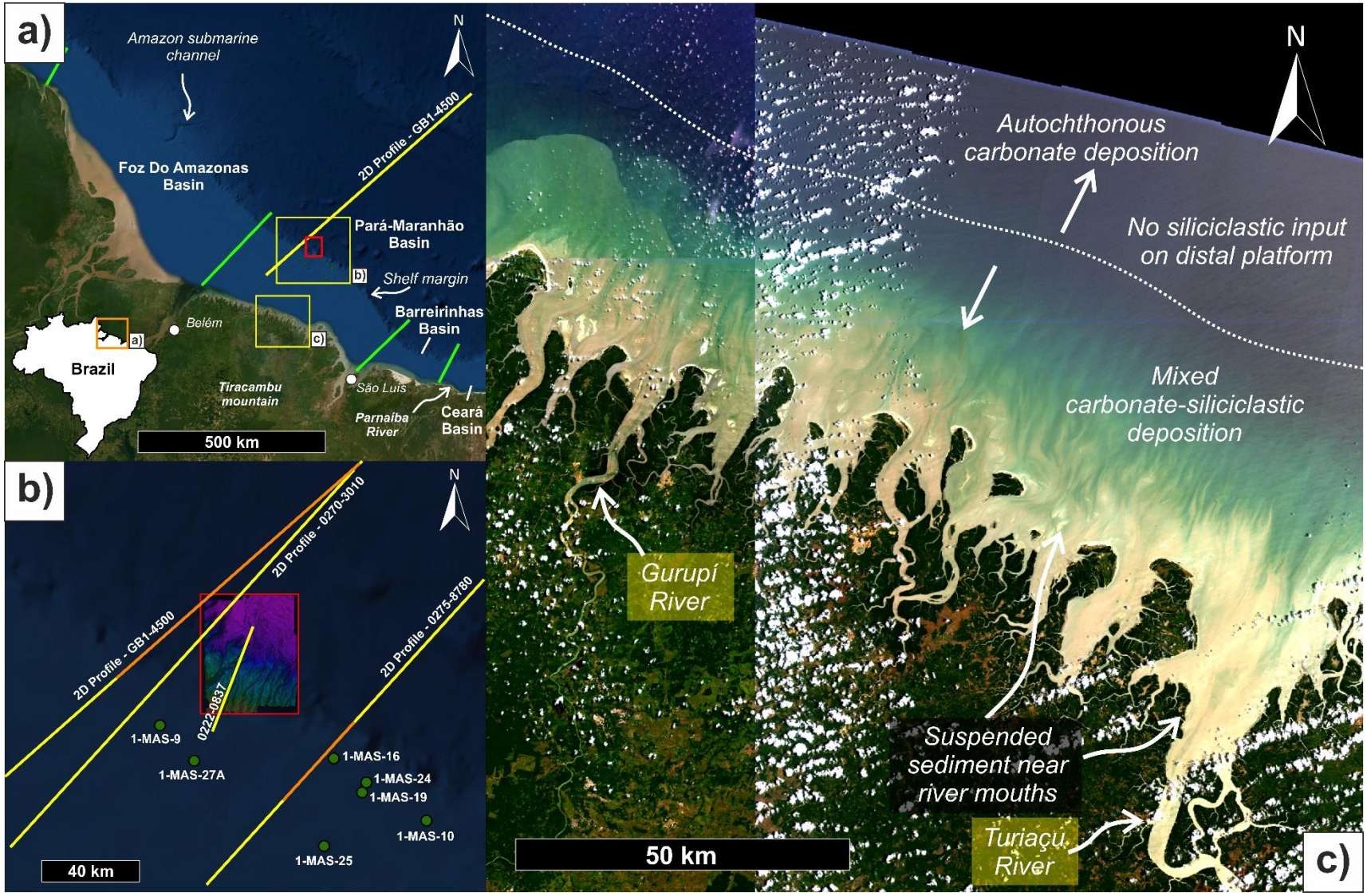

Figure 1. a) Location map of the Brazilian Equatorial Margin highlighting the study area in the Pará-Maranhão (PAMA) Basin. Red rectangle shows the location of the studied 3D seismic survey. Green lines mark basin limits. b) Detailed map showing published 2D seismic profiles crossing the study area, used to correlate the stratigraphy of the interpreted horizons. Profile GB1-4500 is from Henry et al. (2011) and Zalán (2015), profile 0222-0837 is from Fabianovicz (2013) and profiles 0270-3010 and 0275-8780 are taken from Da Silva and Riveiro (2018). Exploration wells near the interpreted 3D seismic survey are shown as green dots. For the detailed well correlation, please refer to Fig. 5. All wells were drilled in shallow waters of the carbonate shelf. c) Multispectral satellite (Sentinel-2) map showing a bathymetric band combination using B4-Red, B3-Green and B1-Ultra blue bands. This map highlights the PAMA offshore areas with suspended siliciclastic sediment and autochthonous carbonate deposits.

1110 **FIGURE 2**

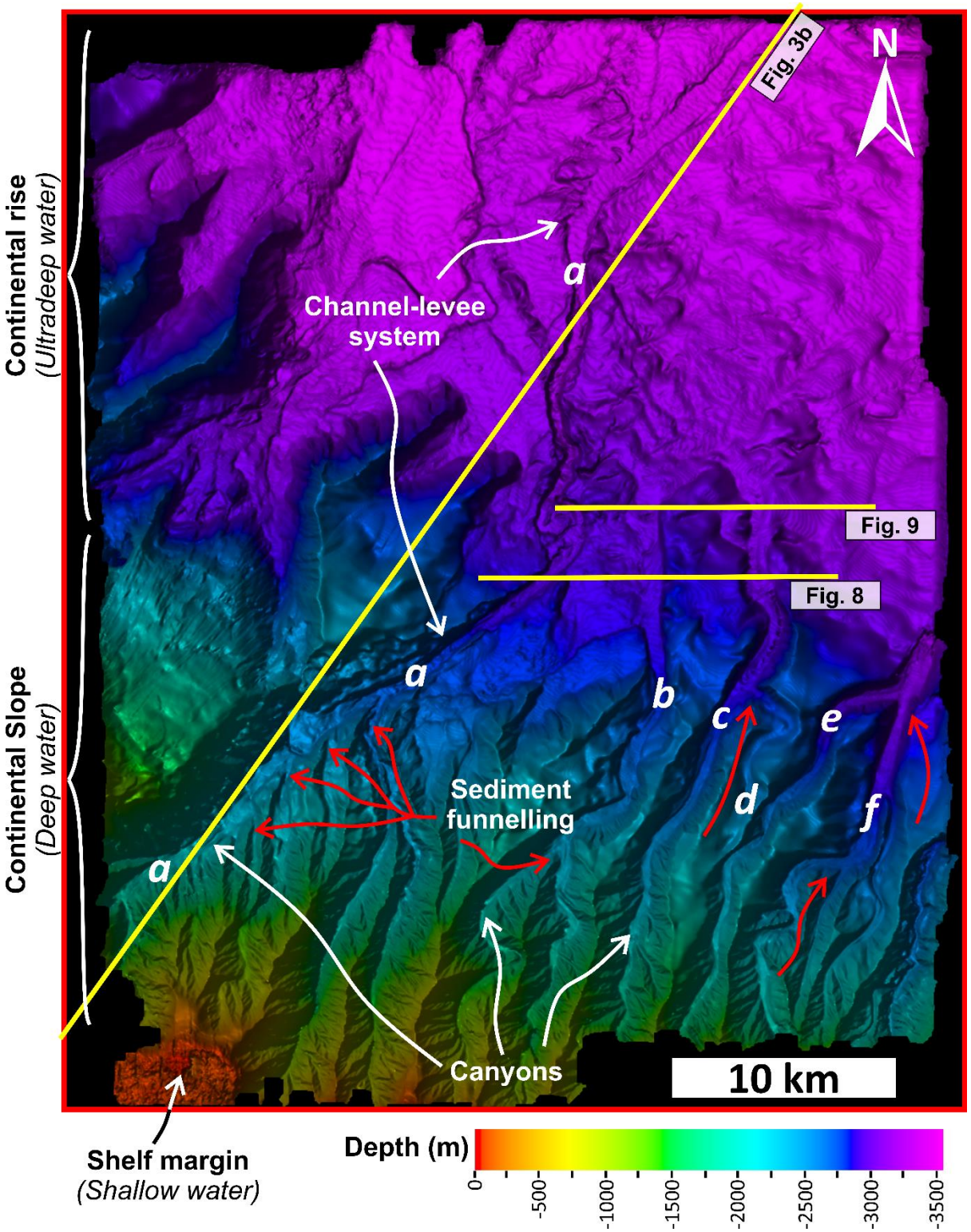

1111

1112 Figure 2. Seafloor relief map highlighting the depositional setting of the PAMA Basin
1113 from the shelf margin to the continental rise. Submarine canyons predominate on the

continental slope, whereas there is a major channel-levee system on the continental rise. Different sediment conduits are labelled from a to f. Red arrows indicate sediment funnelling points within the continental slope. Note the high number of funnelling conduits towards channel *a*.

1118 **FIGURE 3**

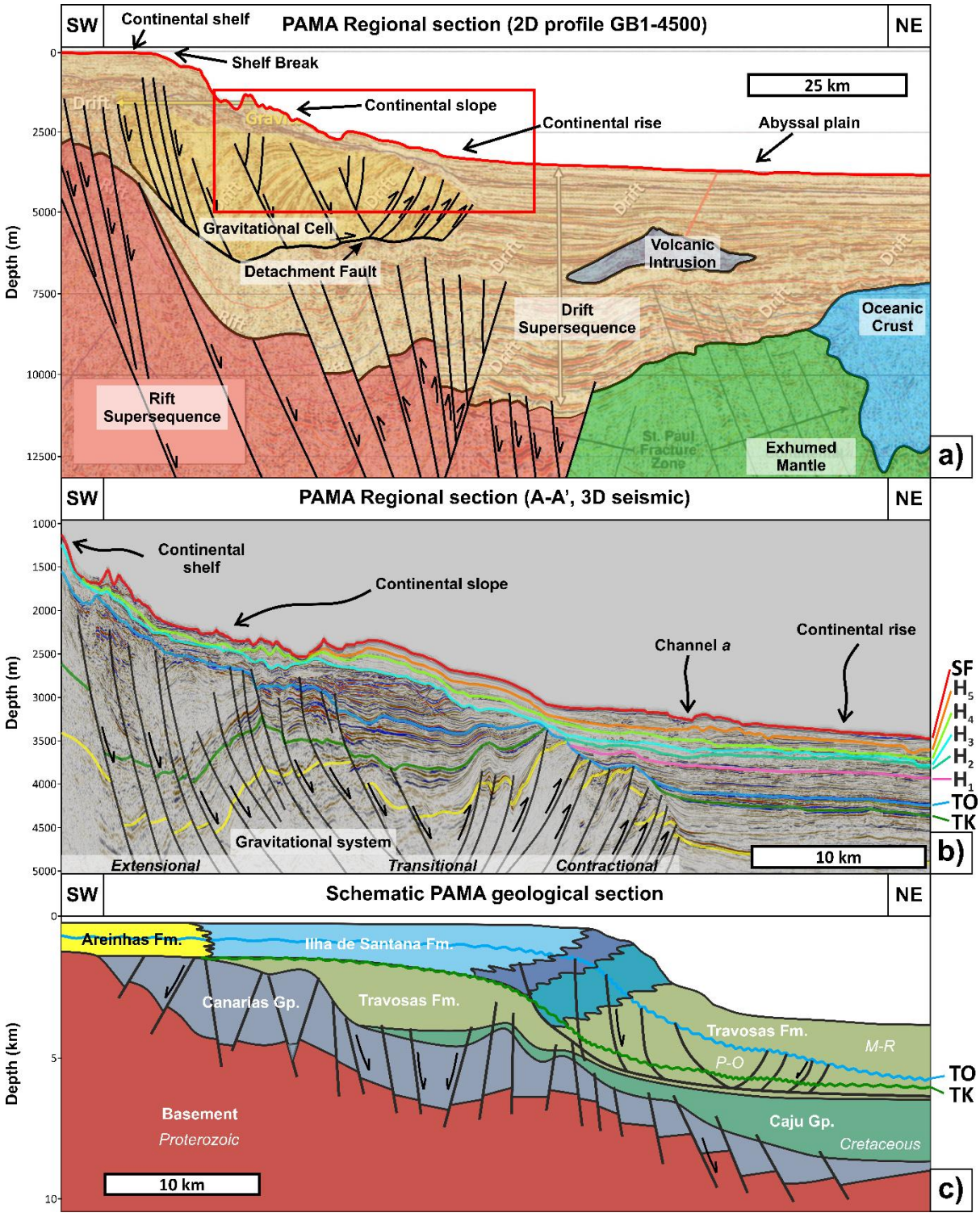

1119

1120 Figure 3. Regional seismic sections depicting the regional stratigraphic units and seismic facies
1121 of the PAMA Basin. a) Reinterpreted 2D seismic profile GB1-4500 from Henry et al. (2011)
1122 and Zalán (2015) displaying the depositional sequences of the basin at the regional scale. A red

1123 rectangle shows the portion of the basin studied in this work, which encompasses the upper
1124 section of the Drift Supersequence above the gravitational cell. Refer to Fig. 1b for location.
1125 b) Seismic section of the 3D seismic survey showing the detailed stratigraphy of the PAMA
1126 Basin. A gravitational system is observed below the Top Oligocene (TO) unconformity
1127 comprising extensional, transitional and contractional sections. Refer to Fig. 2 for location. c)
1128 Schematic section of the PAMA Basin outlining the distribution of the different geological
1129 formations. P-O=Paleocene-Oligocene, M-R=Miocene-Recent. Modified after Brandão and
1130 Feijó (1994).
1131

FIGURE 4

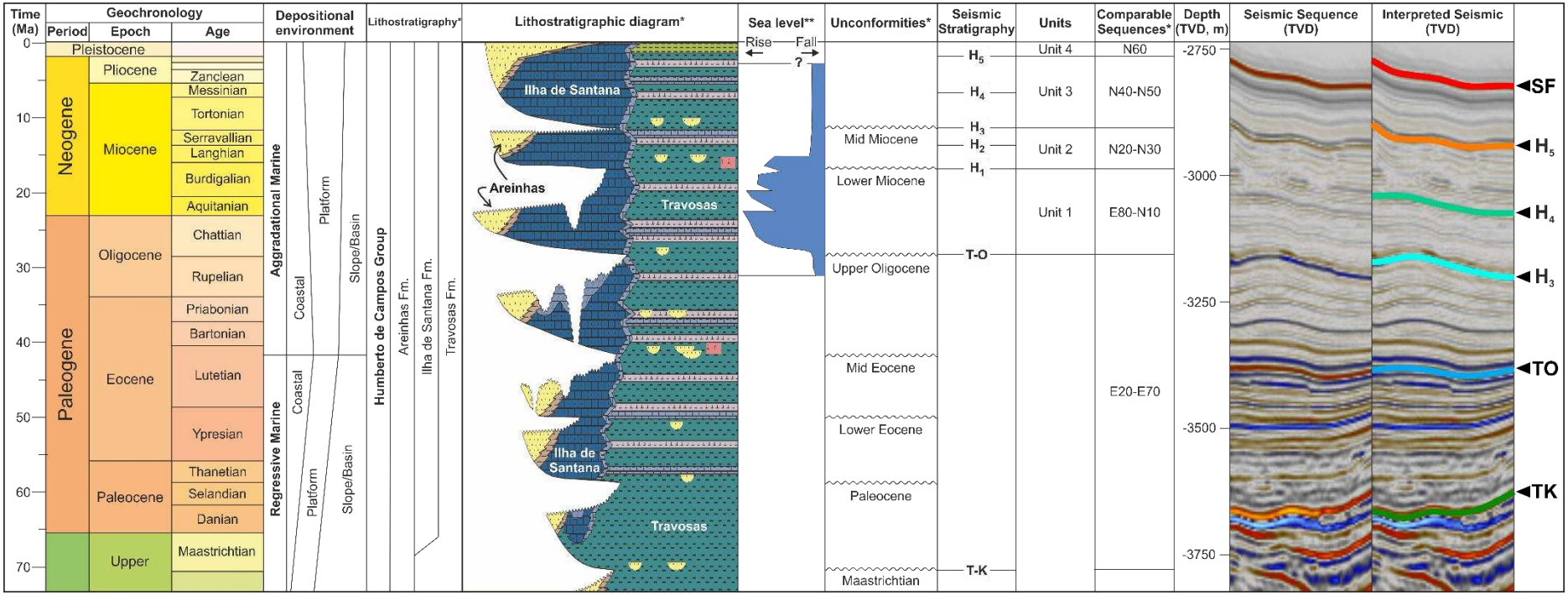

Figure 4. Cenozoic lithostratigraphic chart of the PAMA Basin and its main seismic stratigraphic units. *Comparable sequences, unconformities and lithostratigraphy taken from Soares et al. (2007). **Sea level curve taken from Rossetti et al. (2013) based on data from the Pirabas and Barreiras formations.

1137

FIGURE 5

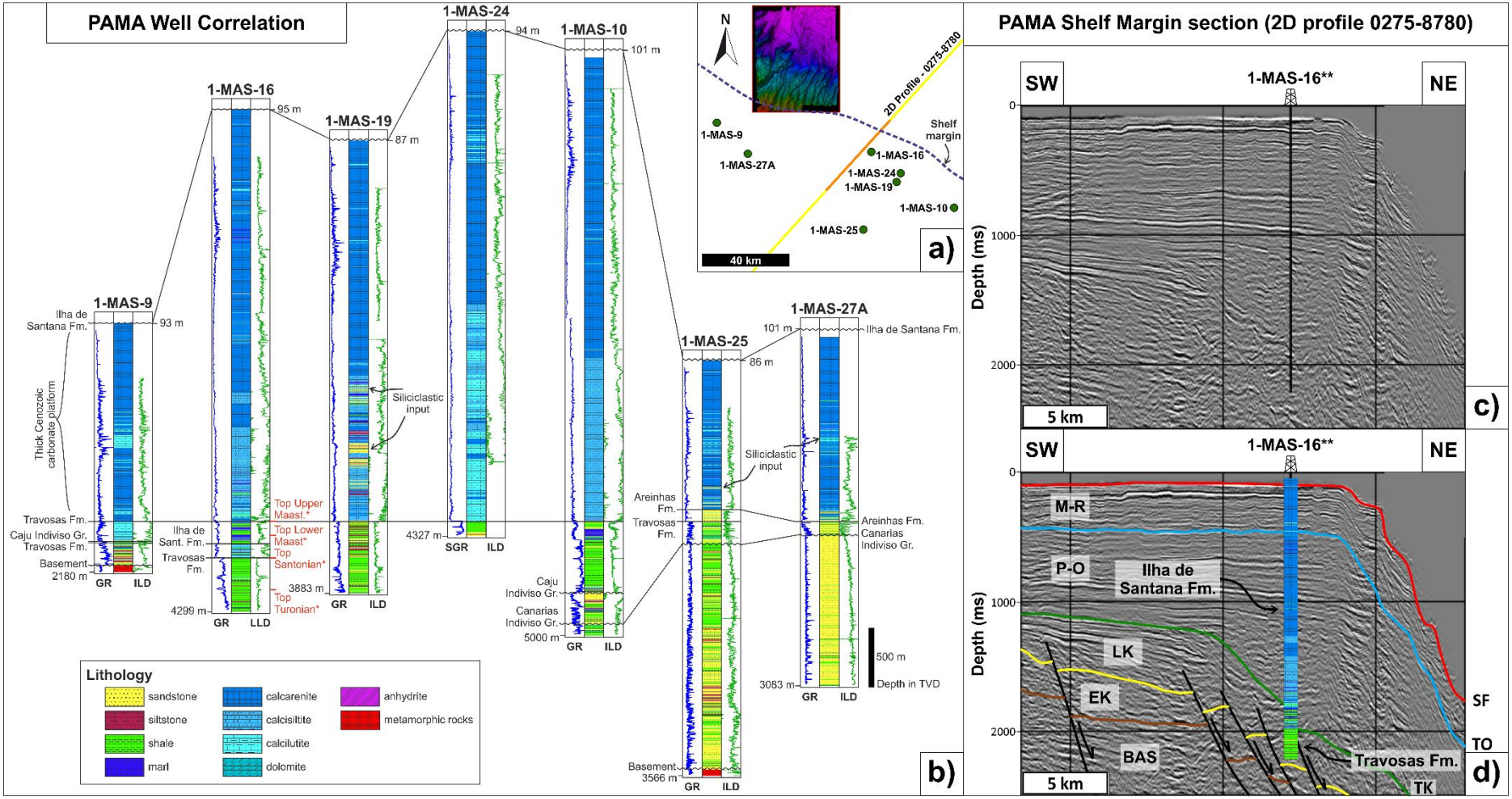

1138

Figure 5. Well correlation panel and seismic sections on the PAMA shelf margin. a) Map of the study area showing the location of wells and seismic data. A blue dashed line shows the shelf margin for reference. b) Well correlation panel for wells 1-MAS-9, 1-MAS-16, 1-MAS-19, 1-MAS-24, 1-MAS-10, 1-MAS-25 and 1-MAS-27A. Well correlation is flattened on the Travosas Formation marker. Information displayed for each well are lithology, Gamma-Ray (GR) and Deep Resistivity (ILD) wireline curves. *Cretaceous ages for well 1-MAS-16 were taken from paleontological data in Piovesan (2008). c) and d) Uninterpreted and interpreted seismic profile 0275-8780 showing the PAMA shelf margin with a thick carbonate platform corresponding to the Ilha de Santana Formation. **Well location is projected. BAS=Basement, EK=Early Cretaceous, LK=Late Cretaceous, P-O=Paleocene-Oligocene, M-R=Miocene-Recent. Modified from Da Silva and Ribeiro (2018).

1148 **FIGURE 6**

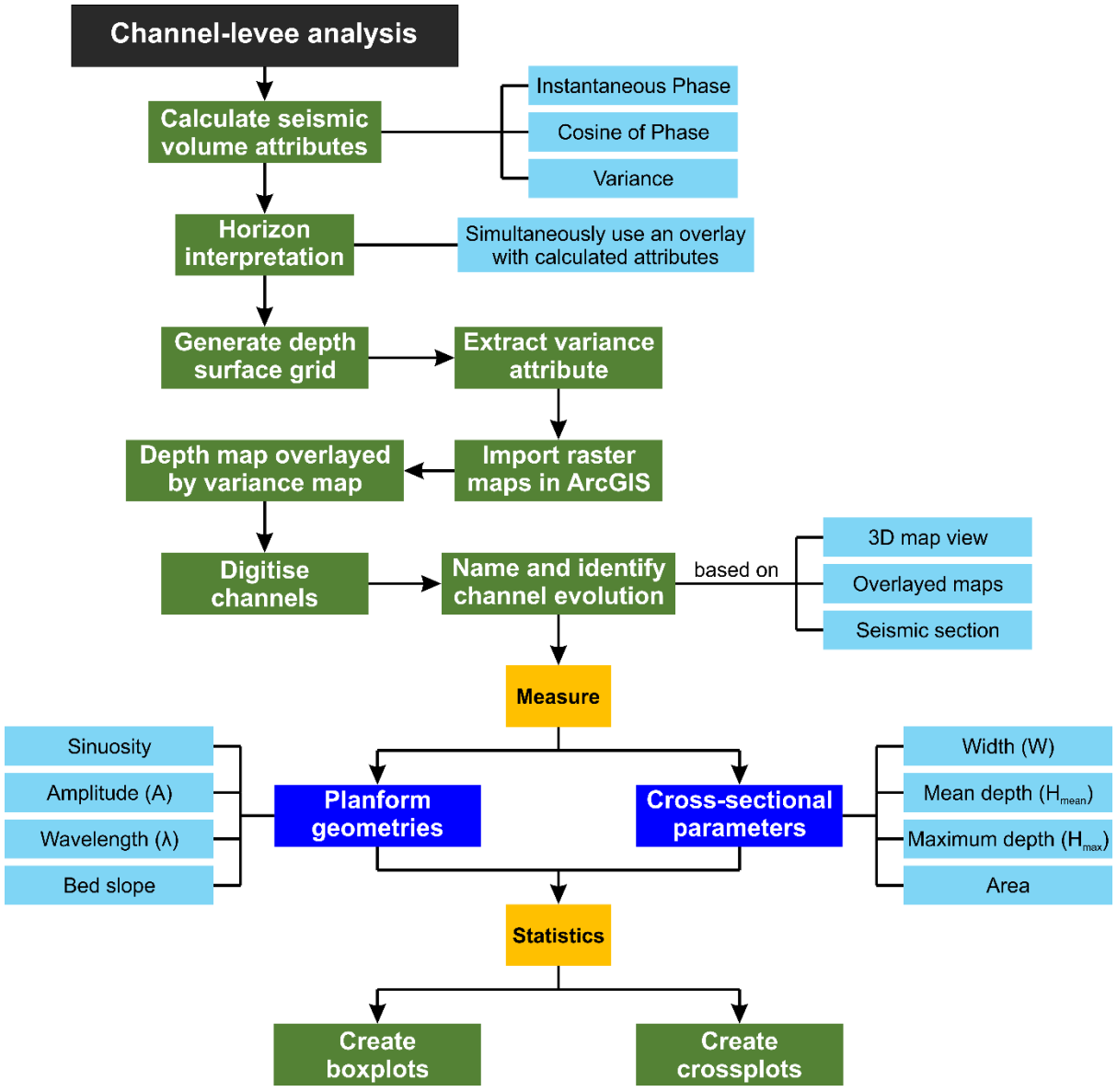

1149

1150 Figure 6. Flowchart summarising the methodology used in this work to identify and analyse

1151 channel-levee systems.

1152

1153 **FIGURE 7**

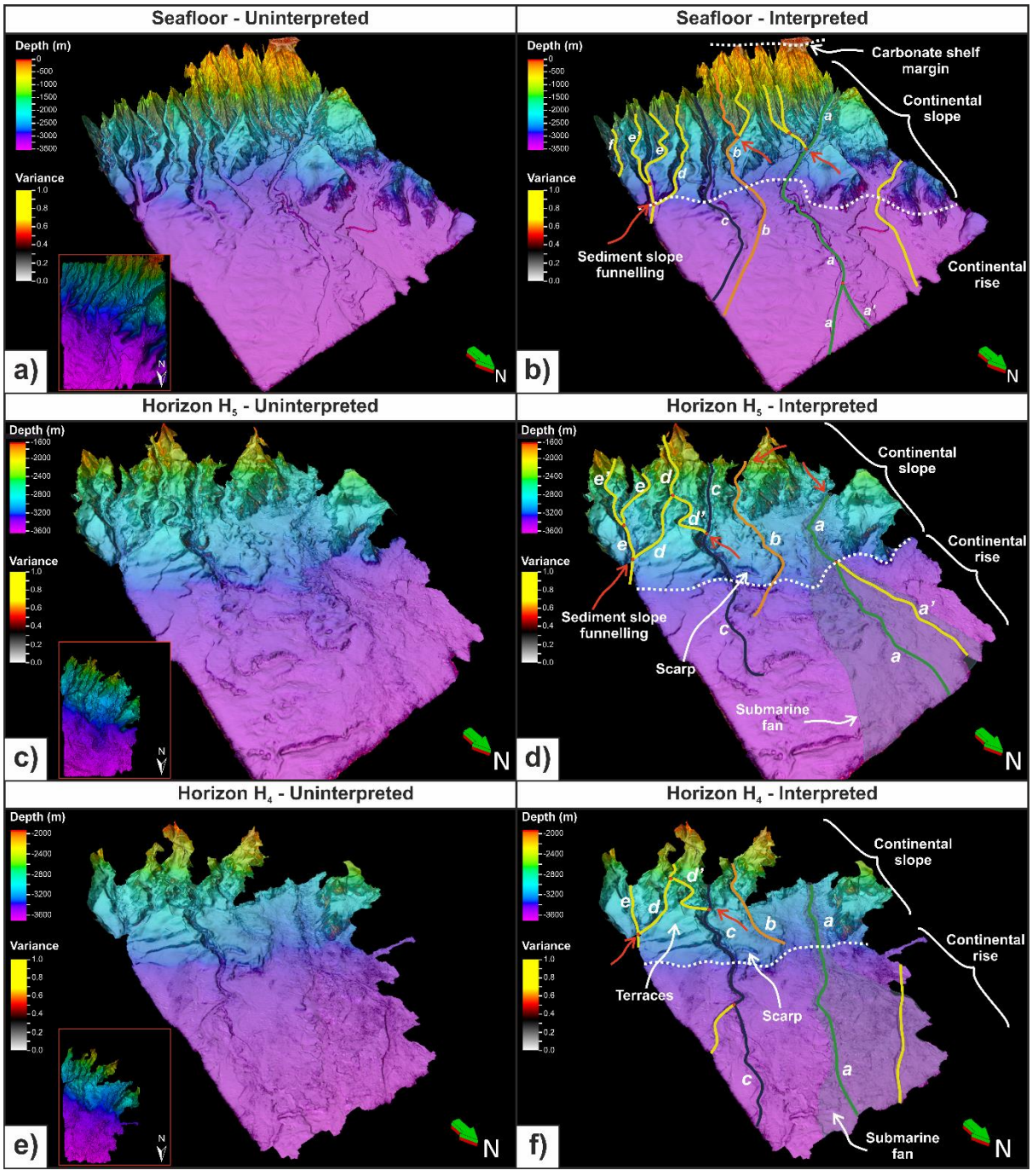

1154

1155 Figure 7. 3D views of blended depth and variance horizon maps at different intervals: Seafloor
1156 (a, b), horizon H_5 (c, d), and horizon H_4 (e, f). Uninterpreted (a, c, e) and interpreted (b, d, f)
1157 maps are shown, and principal morphological features are highlighted in them, including the
1158 channel-levee systems interpreted in this work. Red arrows indicate sediment funnelling points
1159 on the continental slope.

1160 **FIGURE 7. Continued.**

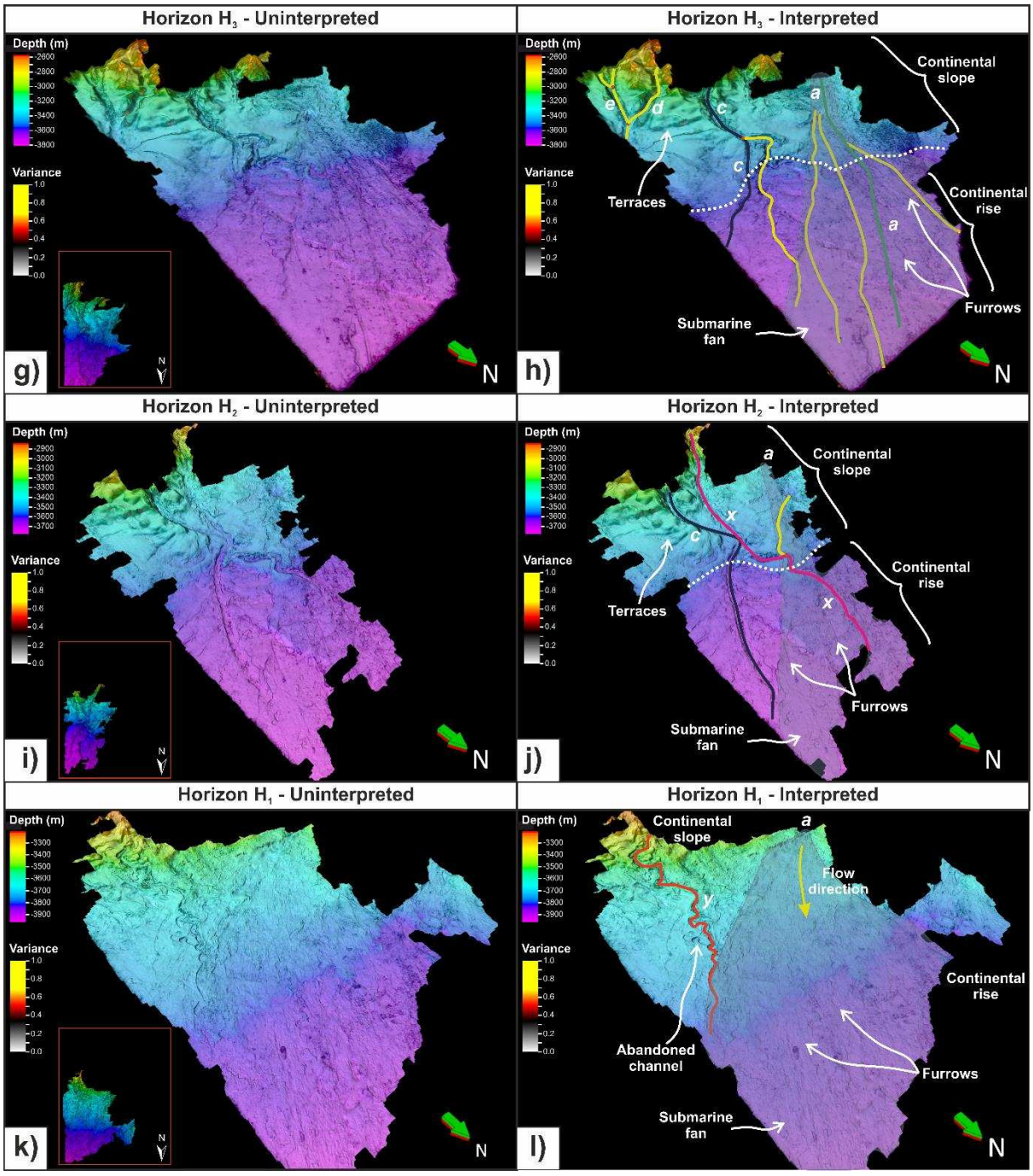

1161

1162 Figure 7. (continued). 3D views of blended depth and variance horizon maps at different
1163 intervals: horizon H_3 (g, h), horizon H_2 (i, j), and horizon H_1 (k, l). Uninterpreted (g, i, k) and
1164 interpreted (h, j, l) maps are shown to highlight main morphological features, including the
1165 channel-levee systems interpreted in this work.

1166 **FIGURE 8**

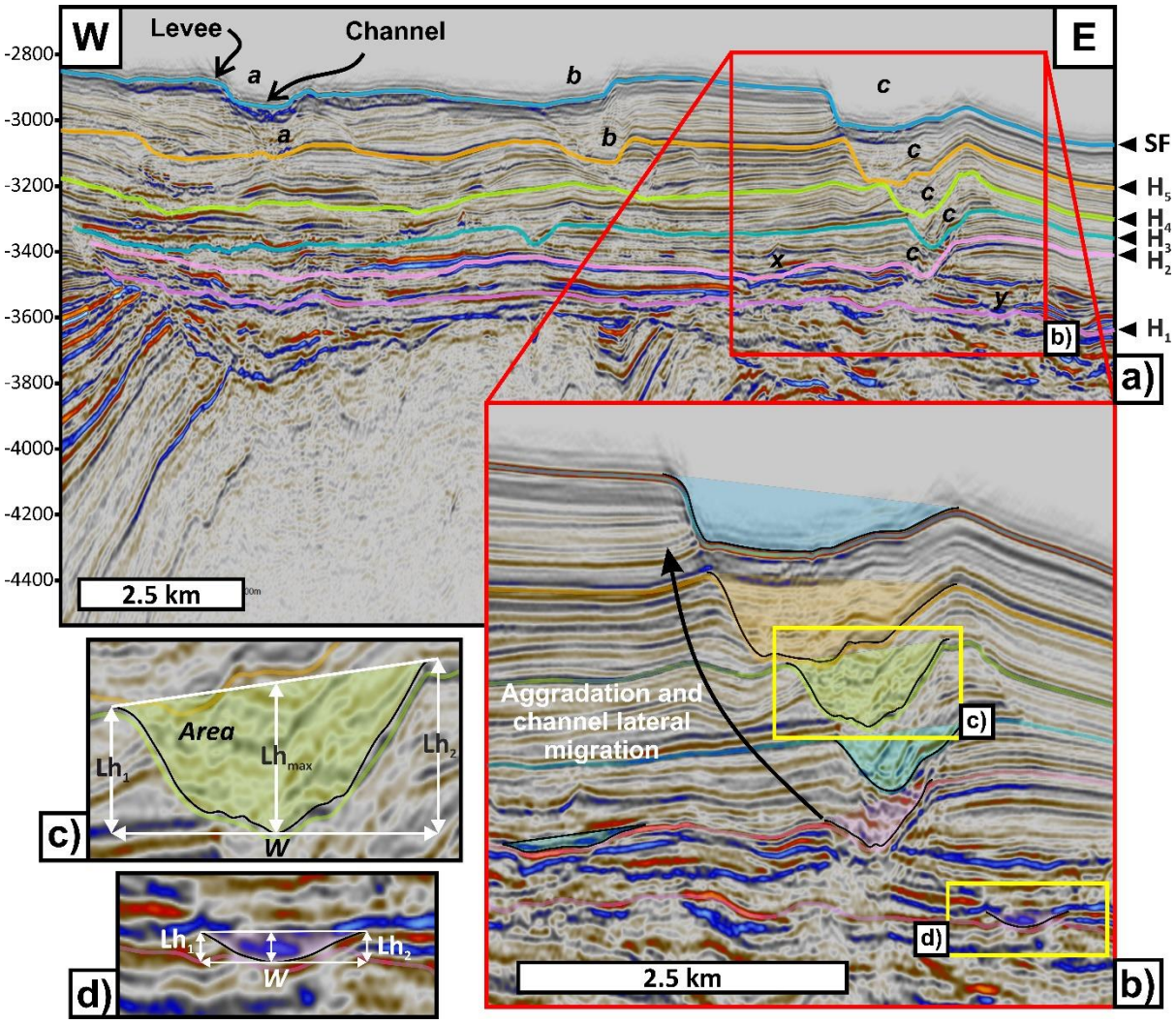

1167

1168 Figure 8. Seismic section showing the channel-levee systems in cross-section and the
1169 way in which geomorphic data were measured. Lh_1 and Lh_2 are the levee heights, which is the
1170 vertical distance between the deepest points (thalweg) of the channel to the two levee crests.
1171 Lh_{max} is the maximum levee height, which is measured as the average height between Lh_1 and
1172 Lh_2, as there is asymmetry in the channels. The parameter W is the channel width, which is
1173 measured between the levee crests.

1174 **FIGURE 9**

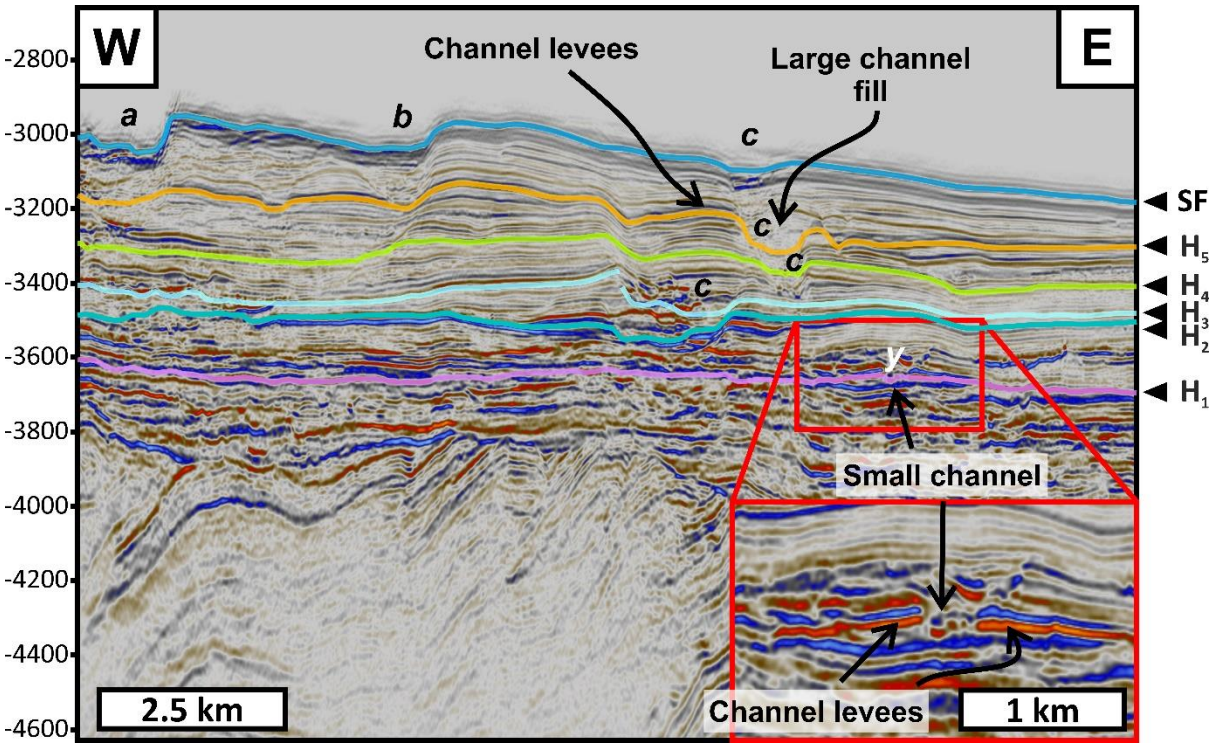

1175

1176 Figure 9. Seismic section showing the difference in cross-sectional scale between
1177 channel-levee systems. Channel y is only about 0.5 km wide and is buried by a low-amplitude
1178 reflection unit. In contrast, channel *c* is three to five times wider than channel *y* and reveals an
1179 aggradational pattern. Both channels have external levees.

1180

1181 **Figure 10**

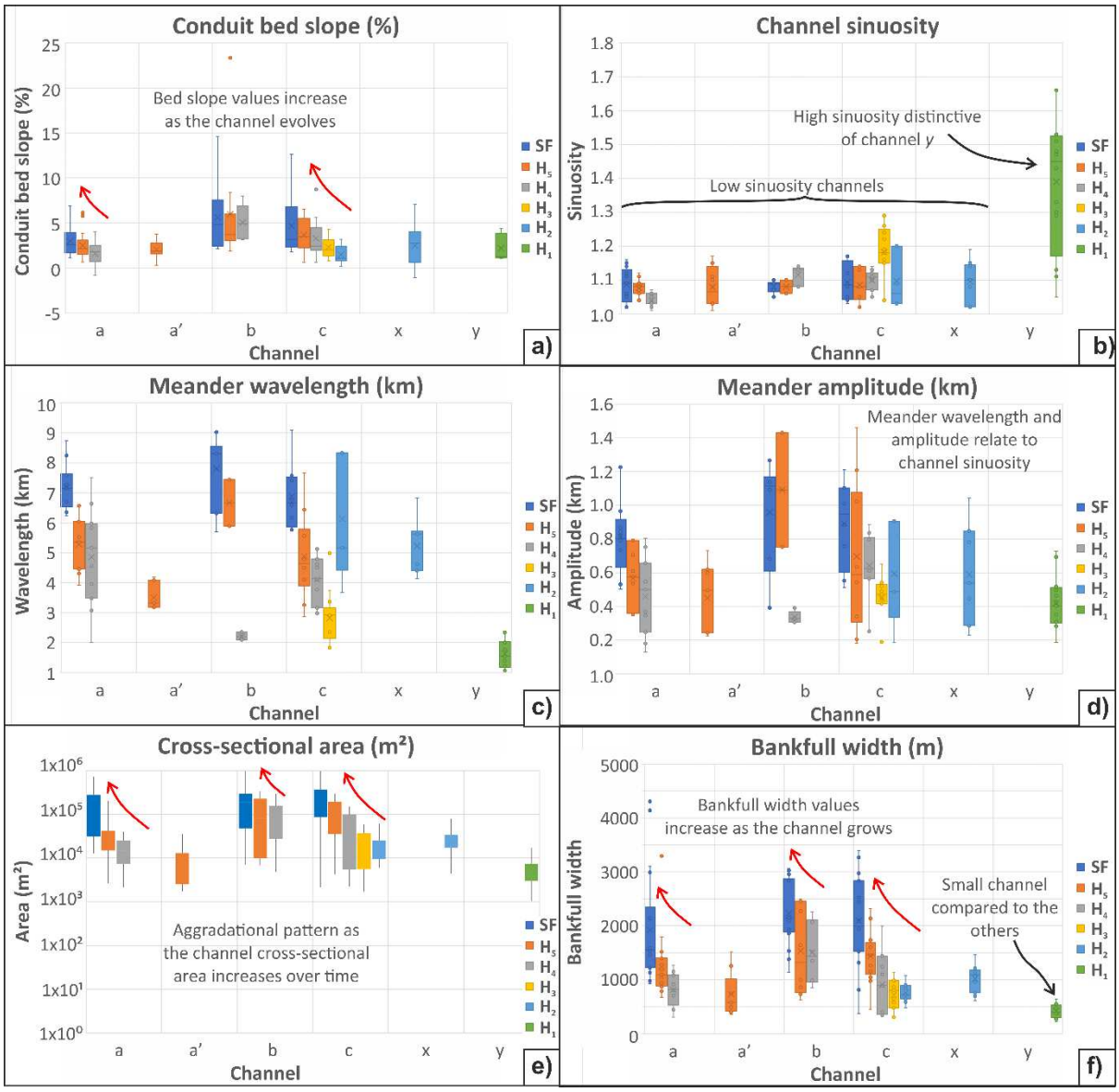

1182

1183 Figure 10. Cross-sectional distribution box plots of the channel-levee systems in the

1184 PAMA Basin. a) Conduit bed slope; b) channel sinuosity; c) meander wavelength; d) meander

1185 amplitude; e) cross-sectional area; and f) bankfull width.

1186

1187

FIGURE 11

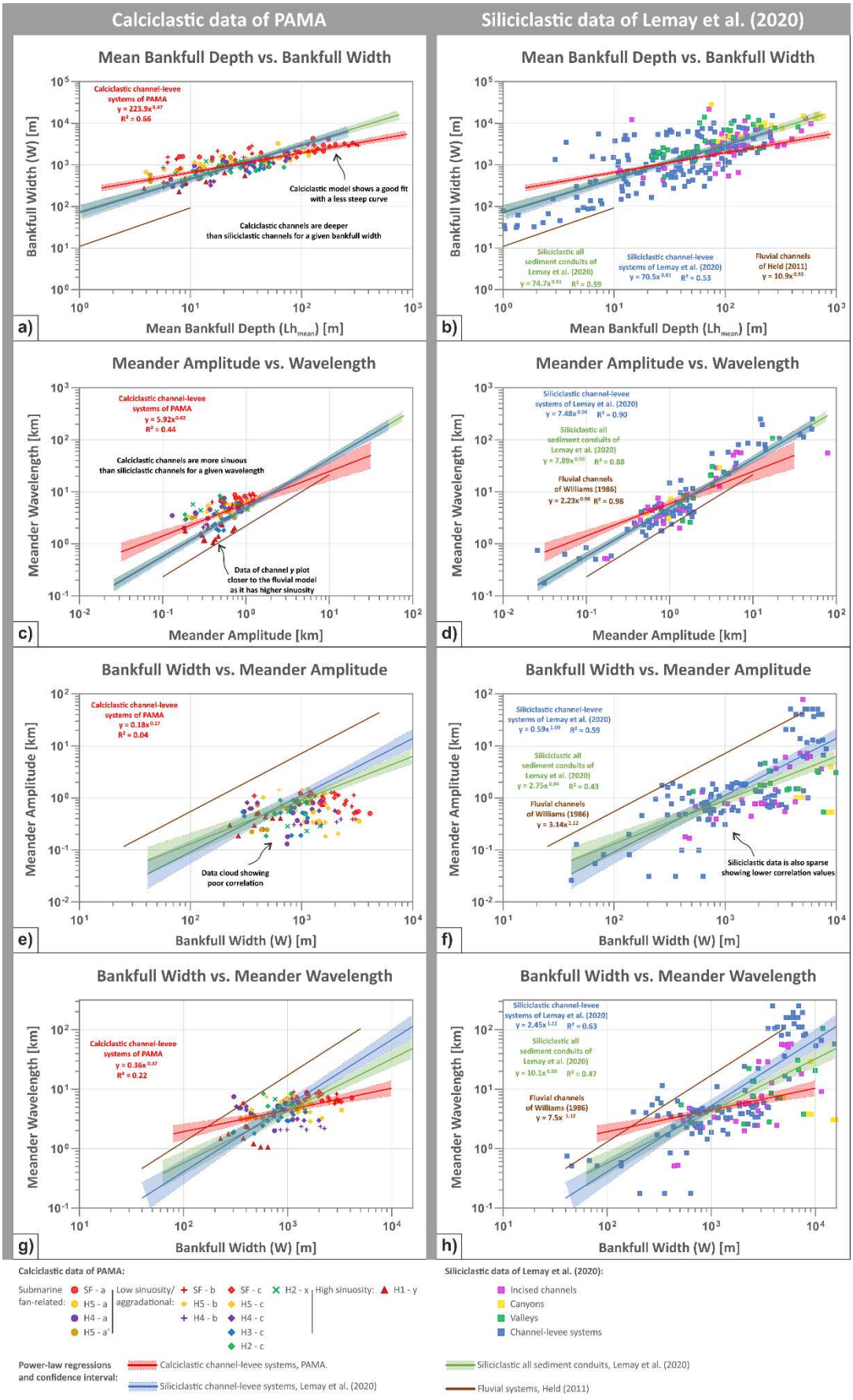

1188

1189 Figure 11. Cross-plots comparing morphometric relationships of calciclastic channel-
1190 levee systems of PAMA and siliciclastic sediment conduits taken from Lemay et al., 2020.
1191 Power-law equations from Williams et al. (1986), Held (2011) and Lemay et al. (2020) are
1192 plotted to compare calciclastic channel-levee systems with the geometries of siliciclastic
1193 submarine and fluvial channels. a and b) Mean bankfull depth (Lh_{mean}) against bankfull width
1194 (W); c and d) meander amplitude vs. meander wavelength; e and f) bankfull width vs. meander
1195 amplitude; and g and h) bankfull width vs. meander wavelength.

1196 **FIGURE 12**

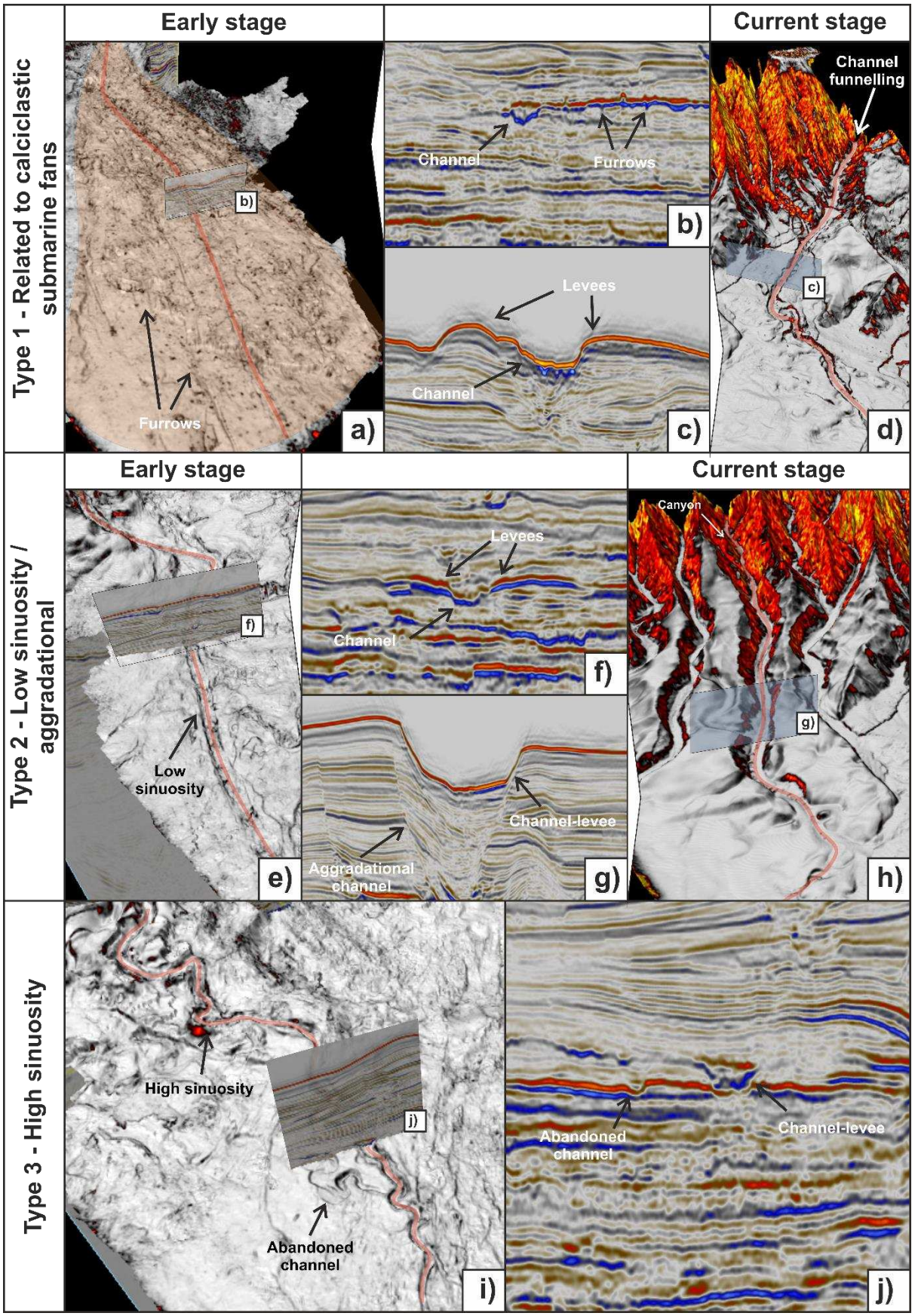

1197

1198 Figure 12. Summary diagram of 3D seismic data showing the main types of channel-
1199 levee systems occurring in the mixed carbonate-siliciclastic depositional system of the PAMA
1200 Basin.

14 Data Availability Statement

The 3D seismic data that support the findings of this manuscript are available from Polarcus. Restrictions apply to the availability of these data, which were used under license for this study. 3D seismic data are available with the permission of Polarcus.

The well data that support the findings of this manuscript were provided by the Brazilian National Agency of Petroleum, Natural Gas and Biofuels (ANP). Restrictions apply to the availability of these data, which were used under a research licence agreement between ANP and the University of Goiás, Brazil.